DME/TACAN Multipath Impact on GNSS L5/E5a Airborne Receivers Part II: Air-Ground Channel Model and Application

Nicolas Gault, Alexandre Chabory, Axel Garcia-Pena, Christophe Macabiau

DME/TACAN Multipath Impact on GNSS L5/E5a Airborne Receivers Part II: Air-Ground Channel Model and Application

NICOLAS GAULT
ALEXANDRE CHABORY
AXEL GARCIA-PENA
CHRISTOPHE MACABIAU
École Nationale de l'Aviation Civile, Toulouse, France

This article is the second part of a two-part manuscript addressing the DME/TACAN multipath impact on the future airborne GNSS L5/E5a receivers. Part I developed the analytical carrier-to-noise-ratio degradation model due to DME/TACAN considering multipath, in the presence of a temporal blanker. Part II introduces an air-ground channel model, that is wide band, geometry based and combines deterministic and statistical parts. The model includes an Okumura-Hata path loss for computing the scatterer illumination, an analytical formula for the additional delay and the mathematical expression of the scattered power. Given the very large number of illuminated scatterers to be considered for an Air-Ground scenario, a statistical simplification of the Physical Optics approach is introduced to simplify the derivation of the scattered powers. The propagation channel model and the mathematical model of the carrier-to-noise-ratio degradation are applied to two low-altitude operational hot-spots, JALTO (Pennsylvania, United-States) and TIXAK (Frankfurt, Germany). It is shown that only a few illuminated scatterers generate a scattered power above the blanking threshold and that the additional carrier-to-noise-ratio degradation generated by the DME/TACAN multipath only is smaller than 0.52 dB.

I. INTRODUCTION

The nominal processing of Global Navigation Satellite System (GNSS) received signals can be affected by noise as well as received additive signals such as multipath (MP) and Radio Frequency Interference (RFI) [1]. GNSS L5/E5a interference environment is predominantly dominated by pulsed interferences such as DME/TACAN and JTIDS/MIDS [2]. In the context of civil aviation, the RFI impact on a GNSS receiver is standardized by the International Civil Aviation Organization (ICAO), by the Radio Technical Commission for Aeronautics (RTCA) in the United States and by the European Organization for Civil Aviation Equipment (EUROCAE) in Europe. In these standards, the RFI impact is usually modeled by the C/N_0 degradation observed at the receiver antenna port when considering ideal the receiver Radio Frequency Front End (RFFE) elements as well as the correlator [1], [2], [3].

To mitigate the impact of the pulsed RFI observed in the L5/E5a band, a temporal blanker in the airborne GNSS receiver RFFE block is assumed to be implemented by the civil aviation standards in Dual-Frequency Multi-Constellation (DFMC) GNSS receivers [1], [4]. The role of the blanker is to set the received signal samples to zero when their instantaneous power envelope exceeds a predefined threshold. The percentage of samples set to zero by the blansker is referred to as the blanking duty-cycle (bdc) and the below-blanker interfering signal-to-noise-ratio as R_I. From R_I and bdc, the value of the C/N_0 degradation solely due to pulsed interferences is derived.

However, no previous work considered any multipath effect which is especially important since echoed pulses could impact the GNSS receiver in the same manner as the direct pulse. In Part I of this two-part manuscript [5], the mathematical expressions for R_I and bdc were updated to provide a statistical average of the C/N_0 degradation including the DME/TACAN MP for a given aircraft position. The application of the new C/N_0 degradation model requires the precise knowledge of the additional delays of the echoed pulses with respect to the direct pulse as well as their scattered powers at the aircraft's antenna port. Therefore, an air-to-ground (AG) aeronautical propagation channel model specifically suitable for RFI analysis is needed.

In the scenarios analyzed in this study, the visible DME/TACAN beacons situated on the ground transmit a signal near the L5 frequency (1176.45 MHz) to an aircraft at an altitude from a few hundred of meters to kilometers and a slant range of a few tens of kilometers. The visible DME/TACAN beacons are referred to as the beacons illuminating at least one scatterer in the Radio Line Of Sight (RLOS) of the aircraft in this article. For this reason, the analyzed scenes are very large and the additional delays of the received echoed pulses are expected to be much longer than the DME/TACAN pulse duration (≈ 10 µs). Therefore, the required aeronautical AG channel model must be wideband, i.e., account for these delays. Furthermore, millions of illuminated scatterers in the aircraft RLOS and in the RLOS of at least one DME/TACAN beacon are potentially generating MP. Consequently, the targeted propagation channel model must be able to cope with a very high number of scatterers without being too computationally expensive, while still being representative from an RFI point of view.

One way forward to derive the required propagation channel model is to analyze the research conducted in the literature for systems with similar constraints such as Unmanned Aerial Vehicles (UAVs). Indeed, given the relatively high altitude of the UAV and the relatively low transmitting antenna height, the AG propagation channel presents similar technical challenges to the ones found in the

targeted channel such as accounting for scattering, reflection, diffraction and shadowing from the illuminated scatterers, reflectors and forests in potentially very complex environments.

With the recent interest in UAVs from both scientific and industry communities, many AG channel models have been developed in the literature and are extensively summarized in numerous surveys [6], [7], [8], [9]. Recent studies address various topics such as extensive measurement campaigns and antenna directivity analysis [10], MP clustering [11] and tracking of the MP components (number, delay, Doppler, scattered power and phase) via channel sounding [11], [12], Line Of Sight (LOS) and non-LOS (NLOS) path probability models [13] and evaluation of reconfigurable intelligent surface (RIS) AG channel characteristics (wideband Ricean fading, Doppler power spectrum and space-time-frequency correlation function) in 3D AG scenarios [14], [15].

AG models that deal with a large number of scatterers and different types of environment (rural, suburban and urban) most commonly found in the literature are measurement-based aeronautical AG channel models. For example, widely cited papers from Matolak *et al.* have introduced a propagation channel model based on an extensive measurement campaign conducted in four different environments across the United-States: over-water, hilly/mountainous, urban and suburban [16], [17], [18]. Another work from Schneckenburger *et al.* have introduced an aeronautical AG Geometrically Based Stochastic Channel Model (GBSCM) based on two L-band (1 GHz – 2 GHz) flight trials conducted in Germany, and the model was validated against measurements [19], [20]. A more recent work from Mielke *et al.* is a measurement-based aeronautical AG channel model based on a measurement campaign realized at C-band, which is above the L-band [12]. Other works found in the literature are the so-called statistical theoretical AG models, generally offering the advantage of being both simple and computationally efficient. They depend on the estimation of their statistical parameters, e.g. the Rice factor, which have to be extracted from measurements [21], [22], [23], [24].

However, even if measurement campaigns always provide highly valuable insights into both the channel and the environment (number of MP, position of the scatterers by means of super-resolution algorithms [25], etc.), they are always extremely expensive and time-consuming and thus limited in terms of number of investigated locations [16], [26]. Furthermore, the applicability of these measurement-based AG channel models to locations where measurements campaigns have not been conducted still needs to be demonstrated. For these reasons, an alternative AG channel model not based on measurement but still coping with the presence of a very large number of illuminated scatterers is proposed in this analysis.

Not measurement-based channel models are deterministic or hybrid deterministic-stochastic (HDS) theoretical channel models. Deterministic or HDS theoretical channel models aim at reproducing the physical electromagnetic (EM) wave propagation in a given environment (deterministic or statistical). Depending on the targeted accuracy, the wave interactions are usually modeled by means of full-wave (or exact) methods such as the Method of Moment (MoM) or by asymptotic methods such as the Uniform Theory of Diffraction (UTD) or Physical Optics (PO). However, to author's best knowledge, no deterministic or HDS theoretical AG channel model is available in the literature.

The deterministic or HDS theoretical channel models that are the most analogous to AG models are the Land-Mobile-Satellite (LMS) models notably designed for GNSS applications. LMS models designed for GNSS applications are analogous to the AG models since they investigate a ground/sky link in the L-band and are wideband since delays of MP must be known to predict the pseudorange measurement error for the estimation of the Position, Velocity and Time (PVT). One example is the propagation channel model developed by Chen *et al.*, a fully deterministic theoretical channel model based on a PO asymptotic approach to investigate the effect of GNSS MP on the airborne GNSS receiver in an airport environment [27]. The PO approach has been numerically validated against MoM and the overall channel performance has been compared against measurements. Another notable example is the Simplified CHannel for Urban Navigation (SCHUN) model proposed by Ait-Ighil [28]. In this model the effect of GNSS MP on GNSS receivers in a urban environment has been investigated using a PO approach in combination with a simplified stochastic urban environment [29]. The SCHUN propagation channel model elements and assumptions have also been numerically validated against MoM and confronted with measurements.

However, the LMS models only investigate a local environment around the receiver where only a few scatterers are generating MP, given the low receiving antenna height. Additionally, the illumination of scatterers differs between LMS and AG scenarios due to the larger elevation angles of the received signals in LMS. Consequently, the set of assumptions considered in the LMS models must be adapted for the AG model. Above all, for AG channels the simulation of the (EM) interactions must be simplified to consider the very large number of illuminated scatterers potentially generating MP across very large scenes.

To summarize, the global motivation of this two-part manuscript is to analyze the impact of DME/TACAN RFI MP signals on the C/N_0 degradation, from the application of the mathematical model proposed in [5]. To apply the C/N_0 degradation model, an AG propagation channel model is needed to obtain the additional delays and the scattered power of the numerous illuminated scatterers in the RLOS of the visible DME/TACAN beacons. Among the various AG propagation channel models already available in the literature, the models that best match the constraints of the targeted AG channel model are the measurement based aeronautical AG models and the simulation based LMS models. However, these two types of channel propagation models do not perfectly respond to the problematic. On the one hand, to the authors' best knowledge, measurement based aeronautical AG models

are typically location dependent or at least their application to other locations where measurement campaigns were not conducted still needs to be demonstrated. On the other hand, in the simulation based LMS models, only reduced environments with only a small number of scatterers due to the low altitude of receiving antenna are considered; however, a very large number of illuminated scatterers are found on the targeted scenarios. Therefore, there is a need for a new HDS, wideband, geometrically based AG propagation channel model.

The objective and the main contribution of this part of the two-part manuscript is thus the proposal of a theoretical HDS wideband AG Geometrically Based Channel Model (GBCM) especially suitable for the AG environment. The specific objective of the proposed AG channel is to provide the scattered powers and the additional delays generated by the illuminated scatterers for a given aircraft position to obtain the statistical average of the C/N_0 degradation as developed in [5]. Moveover, it must be noted that all the mathematical models needed to generate the Channel Impulse Response (CIR) time series for a complete aircraft trajectory are already provided in the manuscript; the only exception is the MP carrier phase which requires an additional analysis/discussion. Therefore, the contribution of this work is not restricted to the proposition of an AG channel model for the DME/GNSS interference analysis. Indeed, the proposed channel model could be easily reused for any other AG system operating in the L band, such as L-band digital aeronautical communication (LDACS), Digital Video Broadcasting–Terrestrial (DBV-T), Digital Audio Broadcasting (DAB), primary or secondary surveillance radar, etc.

Finally, in this work, the proposed AG channel model and the C/N_0 mathematical degradation model presented in [5] are applied to two low-altitude operational hot-spots to provide a numerical example of the statistical average of the additional C/N_0 degradation generated by the consideration of the DME/TACAN MP. Note that a first version of the proposed AG channel model was previously proposed in [30] by the same authors but has been largely modified and enhanced since.

The article is organized as follows. Section II provides a global description of the proposed AG channel model with the introduction of the CIR. Section III introduces the determination of the CIR parameters. Given the large number of illuminated scatterers, section IV proposes a statistical simplification of the classical PO approach to reduce the overall computation time. Section V summarizes the general methodology to obtain the statistical average of the C/N_0 degradation in presence of MP, utilizing the proposed AG channel model and the analytical formulas for R_I and bdc presented in Part I [5]. Section VI is dedicated to the presentation of two numerical applications of the model at two low altitude operational hot-spots: JALTO (Philadelphia, USA) and TIXAK (Frankfurt, Germany). Section VII concludes the analysis.

II. PROPAGATION CHANNEL MODEL DESCRIPTION

In this section, the proposed AG channel model and the CIR are described. The proposed AG channel model investigates a single visible DME/TACAN beacon and aircraft configuration that is illustrated in Fig. 1 (the visible DME/TACAN beacons are referred to as the beacons illuminating at least one scatterer in the Radio Line Of Sight (RLOS) of the aircraft in this article).

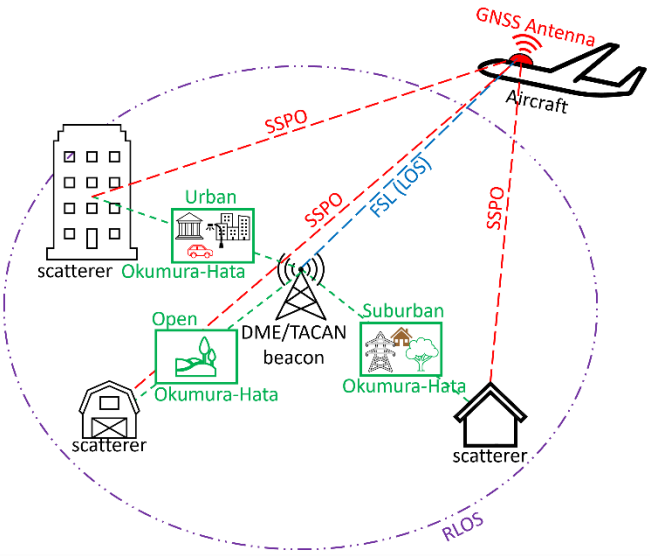

Fig. 1. Illustration of the proposed AG propagation channel model. The blue, green and red dashed lines represent the beacon-to-airborne GNSS antenna, beacon-to-scatterer and scatterer-to-airborne GNSS antenna paths, respectively. The purple dashed line is used to illustrate the RLOS of the DME/TACAN beacon.

The proposed AG channel model considers three paths that are detailed as follows.

The first path is the direct beacon-to-airborne GNSS antenna path represented as a blue dashed line in Fig. 1. It originates from the communication between the visible DME/TACAN beacon and the airborne DME/TACAN transponder, where the signal sent by the beacon is also received by the DFMC GNSS antenna, since both GNSS L5/E5a and DME/TACAN operate in the same frequency band. As the received DME/TACAN signal is not a GNSS (useful) signal, the DFMC GNSS receiver is in fact victim of RFI. In the civil aviation standards, a DME/TACAN beacon servitude (a cylinder of radius 300m centered at the DME/TACAN beacons where no scatterer should be found [31]) is considered and thus the direct signal is assumed to be received without encountering any scatterer (LOS scenario). Therefore, in the proposed AG channel model, the direct signal power is computed only considering Free Space Loss (FSL), as it is currently done in [1].

The second path is the beacon-to-scatterer path represented as a green dashed line in Fig. 1. Indeed, the illuminated scatterers of the visible DME/TACAN must be

considered since they potentially produce echoed pulses which would be considered as additional RFI. Since the altitude of the scatterer centers and the DME/TACAN beacon antenna height are often quite similar, there is a high probability of the beacon-to-scatterer path being obstructed by another scatterer. Therefore, in the proposed AG channel model, the illumination of the scatterers is assumed to follow a Okumura-Hata statistical model [32] where the Obstructed LOS (OLOS) scenarios are considered.

Finally, the third path is the scatterer-to-airborne GNSS antenna path, represented as a red dashed line in Fig. 1. The received scattered power at the receiver antenna output is computed by means of a Statistical Simplification of PO (SSPO) introduced in Section IV and the only loss considered is FSL. This situation represents a worst-case scenario from a RFI impact standardization perspective, since no OLOS/NLOS scenarios are considered which would reduce the power reradiated by the illuminated scatterers in comparison to the (always assumed) LOS scenario. Note that this is also consistent with the geometry of the problem, since the height difference between the scatterer height and the aircraft altitude is large: the ray is much less likely to be obstructed by another scatterer than the beacon-to-scatterer path.

To conclude, since an Okumura-Hata illumination model and a SSPO are assumed, the proposed AG channel model is an HDS model which also depends on the illuminated scatterers exact position for the determination of the scattered powers and additional delays. Therefore, the proposed AG channel model is also a GBCM.

The channel is modeled by means of the time-variant CIR $h_m^{\mathrm{CIR}}(t,\tau)$ which can be expressed as [33],

$$h_m^{\mathrm{CIR}}(t,\tau) = \sum_{n=0}^{N_m(t)} \alpha_m^n(t) e^{j\phi_m^n(t)} \delta\left(t - \tau_m^n(t)\right), \qquad (1)$$

where N_m is the number of MP generated by the visible DME/TACAN beacon m, and $(\alpha_m^n, \phi_m^n, \tau_m^n)$ are the MP normalized amplitude, phase and additional delay, respectively. The index $n = 0$ is associated with the LOS signal. The variable τ is used to convolute the time-variant CIR with the visible DME/TACAN beacon m transmitted signal, $s_m(t)$, to obtain the received signal $r_m(t)$ at the GNSS receiver antenna port. When multiple visible DME/TACAN beacons are visible from the aircraft, the received signal $r_m(t)$ is derived for all the visible beacons and the total received signal is retrieved by summing all $r_m(t)$.

Three important remarks must be highlighted regarding equation (1):

1. The objective of this analysis is to provide a statistical average of the C/N_0 degradation at two operational hot-spots: JALTO and TIXAK. Therefore, only one time epoch, $t = t_0$, is investigated in this study and no time-evolution impact is analyzed. For a single time epoch, $t = t_0$, the carrier phases of two MPs, $\phi_m^n(t_0)$, can be modeled as independent and uniform on $[0,2\pi)$. However, note that if time evolution of the phase was required, the carrier phase modelling should account for time-correlated behavior. For a more detailed discussion on the carrier phase time evolution, the reader is referred to [5].
2. The C/N_0 degradation model accounting for multipath as developed in [5] requires the scattered power P_m^n generated by the illuminated scatterers and not the MP amplitude α_m^n. Therefore in this article, only the analytical expression of P_m^n is provided. The relationship between P_m^n and α_m^n is given by $\alpha_m^n = \sqrt{P_m^n / P_{m,TX}}$, where $P_{m,TX}$ is the transmitted power of the visible DME/TACAN beacon m.
3. To prevent the notations from becoming overly complex, the sub-index m and the upper index n, referring to a single illuminated scatterer in the RLOS of a visible DME/TACAN beacon m, are no longer used for the rest of the article.

To summarize, the objective of the proposed channel model is to determine the number of illuminated scatterers generating MP N (see section III.A), their additional delay τ (section III.C) and scattered power P (section III.F for the exact expression and section IV for the simplification) for any aircraft position from a few information about the illuminated scatterers.

III. DETERMINATION OF THE CHANNEL IMPULSE RESPONSE PARAMETERS

In this section, the number of illuminated scatterers N, the analytical expression of the additional delay τ and the scattered power P of the illuminated scatterers at a given aircraft position are provided. Since P relies on the scattered electric field $\boldsymbol{E_s}$ at the DMFC receiving antenna output, the analytical expression of $\boldsymbol{E_s}$ is also introduced. Given the complexity of the scene (dimension of the scene, number and diversity of the illuminated scatterers etc.), the set of simplifications and assumptions to reach a trade-off between simplicity and realism from an RFI point of view is also presented.

The section is organized as follows. Section III.A presents the assumptions concerning the number N of illuminated scatterers generating MP. Section III.B introduces the illumination model of the illuminated scatterers. Section III.C provides the set of assumptions and the analytical expression of the additional delay τ. Section III.D describes the assumptions for the MP scattered power P. Section III.E is dedicated to derivation of the analytical expression of the scattered electric field $\boldsymbol{E_s}$ in the case of a smooth and heterogeneous scatterer by means of PO. The electric field $\boldsymbol{E_s}$ is used to derive the scattered power P in Section III.F. Section III.G concludes by discussing the limitations of the considered approach.

A. Determination of the Illuminated Scatterers N_m

In this section, the assumptions used for the determination of the illuminated scatterers N_m, namely the RLOS and the building facades, are presented.

RLOS: The illuminated scatterers are assumed to be the scatterers both in the RLOS of the aircraft and in the RLOS of at least one DME/TACAN beacon in this work. An object B is said to be in the RLOS of an object A (and vice versa) when [34]

$$R \leq RLOS(H_A^{\mathrm{AMSL}}, H_B^{\mathrm{AMSL}}),$$

$$RLOS(H_A^{\mathrm{AMSL}}, H_B^{\mathrm{AMSL}}) = \sqrt{(4/3\ R_T + H_A^{\mathrm{AMSL}})^2 - (4/3\ R_T)^2} + \sqrt{(4/3\ R_T + H_B^{\mathrm{AMSL}})^2 - (4/3\ R_T)^2}, \quad (2)$$

where R is the Euclidean distance between A and B, $4/3R_T$ is the effective earth radius, and H_A^{AMSL} and H_B^{AMSL} are the Above Mean Sea Level (AMSL) of object A and B, respectively. The AMSL height of an object A is defined as the relief height at the object's location plus the Above Ground Level (AGL) height of the object A, H_A^{AGL}; in the remaining of this work, if no upper index ASML or AGL is used to specify the height of an object, H, the height is expressed as AGL. Note that this definition of the RLOS assumes that the relief does not intersect with the straight line drawn between the object A and the object B (intersection with other scatterers is already considered in the Okumura-Hata illumination model), which represents a worst-case for our application.

Therefore, using (2) definition, a scatterer is said to be illuminated if the following criteria is satisfied,

$$\begin{aligned} R_1 &\leq RLOS\left(H_{\mathrm{DME}}^{\mathrm{AMSL}}, H^{\mathrm{AMSL}}\right) \text{ and} \\ R_2 &\leq RLOS\left(H_{\mathrm{AC}}^{\mathrm{AMSL}}, H^{\mathrm{AMSL}}\right), \end{aligned} \quad (3)$$

where R_1 is the Euclidean distance between the visible DME/TACAN beacon antenna center and the scatterer center, R_2 is the Euclidean distance between the illuminated scatterer center and the aircraft GNSS antenna center, $H_{\mathrm{DME}}^{\mathrm{AMSL}}$ is the AMSL height of the visible DME/TACAN beacon antenna, $H_{\mathrm{AC}}^{\mathrm{AMSL}}$ is the AMSL height of the aircraft GNSS antenna center, and H^{AMSL} is the AMSL height of the illuminated scatterer.

Building Facade: Within such a large scene in densely populated areas, millions of scatterers of various sorts such as buildings, trees, cars etc. are potentially generating MP. Since buildings facades are assumed to be the elements generating the most powerful MP, only the building facades are considered as scatterers in this analysis. Note that the effect of other elements is considered in the building illumination (section III.B). Therefore, the number of illuminated scatterers N is obtained by counting all the building facades in the RLOS of the visible DME/TACAN beacon.

B. Scatterers illumination

In this section, the assumptions concerning the illumination of the scatterers and the determination of the Okumura-Hata environment are presented.

Scatterers illumination: The illuminated scatterers (see section III.A) are illuminated considering an Okumura-Hata model [32]. The Okumura-Hata model aims at predicting path-loss due to fading and shadowing provoked by the overall environments (buildings, trees, cars, ground relief, electric pylons etc.) in urban, suburban and open environments in the 150-1500 MHz frequency band. For the urban case, the path-loss $L_{\mathrm{H}}^{\mathrm{u,dB}}$ in dB is expressed as

$$L_{\mathrm{H}}^{\mathrm{u,dB}} = 69.55 + 26.16\log(f) - 13.82\log(H_{\mathrm{DME}}) - C_{\mathrm{H}} + [44.9 - 6.55\log(H_{\mathrm{DME}})]\log(R_1), \quad (4)$$

where

$$C_{\mathrm{H}} = 3.2(\log(11.75H))^2 - 4.97, \quad (5)$$

and f is the carrier frequency in MHz. For the suburban environments, the path-loth $L_{\mathrm{H}}^{\mathrm{su,dB}}$ in dB is given by

$$L_{\mathrm{H}}^{\mathrm{su,dB}} = L_{\mathrm{H}}^{\mathrm{u,dB}} - 2\left(\log\left(\frac{f}{28}\right)\right)^2 - 5.4, \quad (6)$$

and for the open environments, the path-loss $L_{\mathrm{H}}^{\mathrm{o,dB}}$ in dB is

$$L_{\mathrm{H}}^{\mathrm{o,dB}} = L_{\mathrm{H}}^{\mathrm{u,dB}} - 4.78(\log(f))^2 + 18.33\log(f) - 40.94. \quad (7)$$

Determination of the Okumura-Hata environment: When no other illuminated scatterer exists along the direct path from the visible beacon to the illuminated scatterer, the illuminated scatterer is considered to be in LOS, and consequently in an open environment in this analysis and (7) applies. The illuminated scatterers having a direct path obstructed by other illuminated scatterers are either considered to be in a urban or a suburban environment and either (5) or (6) applies, depending on the density of buildings at the DME/TACAN beacon localization. Fig. 2 provides an example of the Okumura-Hata environment determination where the green illuminated scatterer obstructs the red illuminated scatterer.

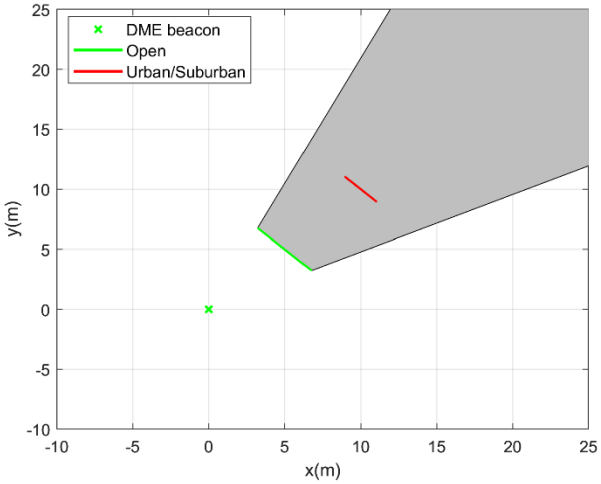

Fig. 2. Example of the proposed Okumura-Hata environment determination.

C. Analytical Expression of The Multipath Additional Delay τ

In this subsection, the assumptions used for the additional delay computation, namely the first-order interaction and the earth flat without bending, are first presented. Second, the analytical expression of the additional delay τ is provided.

First-order Interaction: To simplify the analysis, the illuminated scatterers can only scatter the field coming from the visible DME/TACAN beacon's antenna and not from any other illuminated scatterer.

Flat Earth And Without Refraction: To simplify the model, the Earth is considered as flat for the additional delay analysis. Furthermore, all the paths are considered as straight lines, meaning that tropospheric refraction is not considered.

Considering the previous assumptions, the formula of the additional delay τ of the echoes with respect to the LOS signal is given by

$$\tau = \frac{R_1 + R_2 - D}{c}, \tag{8}$$

where R_1 and R_2 are defined in (3), D is the distance between the visible DME/TACAN beacon antenna center and the aircraft GNSS antenna center (direct path) and c is the free-space speed of light.

D. Assumption For The Multipath Scattered Power P

In this section, the assumptions used for the scattered power P, namely the PO approach, the far-field propagation model, the scatterer orientation and the scatterers composition and shape, are provided.

PO approach: PO is assumed for modelling the EM interactions. Instead of solving rigorously the Maxwell's equation as it is done for the full-wave methods (Method of Moments, Finite Difference in Time Domain etc.), PO is an asymptotic method where the Maxwell equations are solved by means of the determination of the approximated currents and the use of the Stratton-Chu integrals [35]. Asymptotic methods are much faster and cost-efficient than the Full-Wave methods and are thus more suitable for the very large number of illuminated scatterers considered in this study. Note that PO is only valid for scatterers larger than three wavelengths ($\approx$ 75 cm) which is always true for the buildings facade. PO has also been validated against measurements in [36].

Far-field Propagation Model: The scattered power P derivation is made assuming a far-field propagation model, meaning that the illuminated scatterer must be in the far-field of the visible DME/TACAN beacon antenna and that the aircraft must be in the far-field of the obstacle. Indeed, the computation of the Stratton-Chu integrals is faster in that case while still being valid [37]. An object A is in the far-field of an object B if

$$R \geq \frac{2L^2}{\lambda}, \tag{9}$$

where R is the distance between A and B, L is the largest dimension of object A and λ is the wavelength associated with the DME/TACAN carrier frequency.

In the case where the illuminated scatterer is too large to comply with this condition, the illuminated scatterer is divided in smaller elements such that every elements respect the far-field condition. Fig. 3 provides an example of that process, where the initial illuminated scatterer is divided three times.

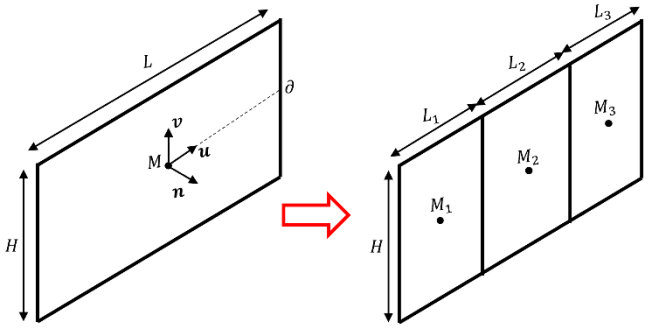

Fig. 3. Example of the proposed methodology to ensure that the far-field condition is always respected.

In Fig. 3, L and H are the length and the AGL height of the scatterer, M is the scatterer center, $\boldsymbol{n}$ is the outgoing normal vector to the scatterer, $\boldsymbol{u}$ is the unit vector originating from M and terminating at the scatterer boundary ∂ and $\boldsymbol{v}$ is the unit vectors completing the orthonormal basis.

Scatterer Orientation: Considering a East-North-Up (ENU) frame $(\boldsymbol{x}, \boldsymbol{y}, \boldsymbol{z})$ centered at DME/TACAN beacon antenna electrical phase center (see Fig. 5), the scatterer horizontal orientation is defined as the angle between $\boldsymbol{n}$ and $\boldsymbol{x}$ and the vertical orientation is defined as the angle between $\boldsymbol{v}$ and $\boldsymbol{z}$. The scatterer are assumed to be perpendicular to the ground in this work and thus the vertical angle is always equal to 0° ($\boldsymbol{z} = \boldsymbol{v}$).

Scatterer Composition and Shape: To simplify the analysis, the illuminated scatterers are assumed to be composed by one dominant material among four different available materials: metal, concrete, brick, and wood, and, in addition to the dominant material, by windows composed of glass. The materials are modeled as slabs characterized by a thickness t_h and a complex relative permittivity ϵ_r. The four dominant materials have been chosen to represent real-life scenarios while covering a wide range of ϵ_r values [38]. The values of t_h and ϵ_r for the 4 dominant materials and the glass are provided in the two first columns of Table I.

TABLE I
Permittivity ϵ_r, thickness t_h and $|h_v(0,0)|$ for the 5 materials

Material	ϵ_r	t_h (cm)	$\lvert h_v(0,0)\rvert$
Metal	-	-	0.65
Concrete	6.5-j0.4	30	0.74

Brick	3.75-j0.68	30	0.76
Wood	1.42-j0.02	30	1.44
Glass	5-j0.025	0.5	-

Finally, the shape of the building facades is assumed to be a perfect rectangle in this work.

E. Derivation of The Scattered Field $\boldsymbol{E_s}$ In The Case of a Smooth and Heterogeneous Scatterer

The derivation of the scattered field $\boldsymbol{E_s}$ at the aircraft GNSS antenna port in the case of a smooth and heterogeneous is necessary in order to obtain the MP power P. In this article, a scatterer is said smooth if no small details with respect to the wavelength are represented and heterogeneous if it is composed of a combination of one material (metal, brick, concrete or wood) and at least one window (composed of glass). Fig. 4 shows an example of a rectangular smooth and heterogenous building facade from the ENAC campus, where the grey elements are composed of one of the dominant materials and the blue elements are made of glass.

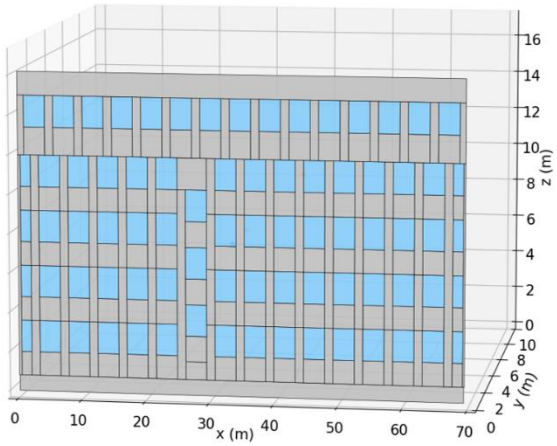

Fig. 4. Example of a rectangular smooth and heterogeneous building facade from the ENAC campus building. Grey: dominant material, blue: glass.

Scene presentation and notation: The visible DME/TACAN beacon antenna electrical phase center (represented by A), illuminated scatterer center (M) and the aircraft GNSS antenna electrical phase center (represented by B) scene are presented in Fig. 5.

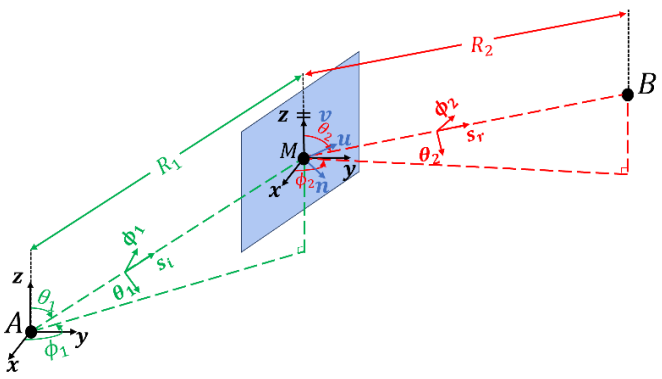

Fig. 5. Representation of the DME-Scatterer-Aircraft scene.

In Fig. 5, $\boldsymbol{s_i}$ and $\boldsymbol{s_r}$ are the unit vector representing the direction of incidence and observation, respectively,

$$\begin{aligned} \boldsymbol{s_i} &= \frac{\boldsymbol{AM}}{R_1}, \\ \boldsymbol{s_r} &= \frac{\boldsymbol{MB}}{R_2}, \end{aligned} \tag{10}$$

where $(\boldsymbol{s_i}, \boldsymbol{\theta_1}, \boldsymbol{\phi_1})$ and $(\boldsymbol{s_r}, \boldsymbol{\theta_r}, \boldsymbol{\phi_r})$ are the spherical incident and reflected frame, respectively. Furthermore, θ_1, ϕ_1 and θ_2, ϕ_2 are the spherical-coordinate angles for the direction of incidence and observation, respectively.

Derivation of the Scattered Field $\boldsymbol{E_s}$: For the smooth and heterogenous scatterers, the PO approach implies to mesh the illuminated scatterer in a number Γ of elements such that each element is smooth and homogeneous. In this article, a scatterer is said homogenous if it is composed of only one material (here metal, concrete, brick, wood or glass). After meshing, the scattered field $\boldsymbol{E_s}$ is given by

$$\boldsymbol{E_s} = \sum_{\gamma=1}^{\Gamma} \boldsymbol{E_s^{sh,\gamma}}, \tag{11}$$

where $\boldsymbol{E_s^{sh,\gamma}}$ is the scattered field of each smooth and homogeneous elements γ.

The scattered field $\boldsymbol{E_s^{sh,\gamma}}$ for a smooth and homogeneous element is derived in the following. Note that the upper-index γ is no longer used in the derivation to prevent the notations from becoming overly complex. The scattered field $\boldsymbol{E_s^{sh}}$ at the aircraft GNSS antenna electrical phase center is derived by means of the far-field formulation of the Stratton-Chu integrals [37]

$$\begin{aligned} \boldsymbol{E_s^{sh}} = j\frac{k_0}{4\pi}\frac{e^{-jk_0R_2}}{R_2}\Bigg\{\zeta_0 \boldsymbol{s_r} \times \Bigg[\boldsymbol{s_r} \times \iint_S \boldsymbol{J_e}(\boldsymbol{M'}) e^{jk_0 \boldsymbol{s_r}.\boldsymbol{r'}} dS(M')\Bigg] \\ + \boldsymbol{s_r} \times \iint_S \boldsymbol{J_m}(\boldsymbol{M'}) e^{jk_0 \boldsymbol{s_r}.\boldsymbol{r'}} dS(M')\Bigg\}, \end{aligned} \tag{12}$$

where $k_0 = \frac{2\pi}{\lambda}$ is the wave number, ζ_0 is the free-space impedance, S is the surface of the scatterer, M' is a point of the obstacle, $\boldsymbol{r'} = \boldsymbol{MM'}$ is the vector from the center of the obstacle M to the point M', $\boldsymbol{J_e}(\boldsymbol{M'})$ and $\boldsymbol{J_m}(\boldsymbol{M'})$ are the electric and the magnetic equivalent currents generated at the point M', respectively. In the framework of PO, $\boldsymbol{J_e}(\boldsymbol{M'})$ and $\boldsymbol{J_m}(\boldsymbol{M'})$ are expressed as

$$\begin{aligned} \boldsymbol{J_e}(\boldsymbol{M'}) &= \frac{1}{\zeta_0}\left(\boldsymbol{n} \times (\boldsymbol{s_i} \times \boldsymbol{E_i}(\boldsymbol{M'}) + \boldsymbol{n} \times \boldsymbol{s_i} \times \mathbf{R}\boldsymbol{E_i}(\boldsymbol{M'})\right) \\ \boldsymbol{J_m}(\boldsymbol{M'}) &= -\boldsymbol{n} \times \boldsymbol{E_i}(\boldsymbol{M'}) - \boldsymbol{n} \times \mathbf{R}\boldsymbol{E_i}(\boldsymbol{M'}). \end{aligned} \tag{13}$$

Furthermore, $\boldsymbol{s_r^{sp}}$, the direction of specular reflection, is given by

$$\boldsymbol{s_r^{sp}} = \boldsymbol{s_i} + 2\cos(\theta_i)\,\boldsymbol{n}, \tag{14}$$

where θ_i is the angle between $\boldsymbol{s_i}$ and $-\boldsymbol{n}$, $\mathbf{R}$ is the Dyadic Fresnel reflection coefficient of the slab [39] and $\boldsymbol{E_i}(\boldsymbol{M'})$ is the vertically polarized electric incident field generated by the DME/TACAN beacon at point M'. Moreover, $\boldsymbol{E_i}(\boldsymbol{M'})$ is expressed as

$$\boldsymbol{E_i}(\boldsymbol{M'}) = \sqrt{\frac{8\pi L_{\mathrm{H}} P_{TX} G_{TX}(\theta_1)\zeta_0}{\lambda^2}}\, e^{-jk_0 R_1}\boldsymbol{\theta_1} = E_i^0\boldsymbol{\theta_1}, \tag{15}$$

where L_{H} is either the linear open, suburban or urban Okumura-Hata path loss as defined in (5),(6) and (7), P_{TX} is the transmitted power of the DME/TACAN beacon and G_{TX} is the gain of DME/TACAN beacon's transmitting antenna.

The incident field corresponds to a plane wave on the surface [27]. Therefore, since the scatterer is homogeneous and rectangular, the double integrals in (12) is given by

$$\begin{aligned}\iint_S \boldsymbol{J_e}(\boldsymbol{M'})\, e^{jk_0 \boldsymbol{s_r}.\boldsymbol{r'}} dS(M') &= \boldsymbol{J_e}(\boldsymbol{M}) LH \mathrm{sinc}\left(k_0\frac{UL}{2}\right)\mathrm{sinc}\left(k_0\frac{VH}{2}\right)\\ \iint_S \boldsymbol{J_M}(\boldsymbol{M'})\, e^{jk_0 \boldsymbol{s_r}.\boldsymbol{r'}} dS(M') &= \boldsymbol{J_m}(\boldsymbol{M}) LH \mathrm{sinc}\left(k_0\frac{UL}{2}\right)\mathrm{sinc}\left(k_0\frac{VH}{2}\right),\end{aligned} \tag{16}$$

where U and V are expressed as

$$\begin{aligned} U &= (\boldsymbol{s_r} - \boldsymbol{s_i})\cdot\boldsymbol{u}\\ V &= (\boldsymbol{s_r} - \boldsymbol{s_i})\cdot\boldsymbol{v}.\end{aligned} \tag{17}$$

Furthermore, combining (13) with (15) yields

$$\begin{aligned}\boldsymbol{J_e}(\boldsymbol{M}) &= \frac{E_i^0}{\zeta_0}\boldsymbol{n}\times\left[\boldsymbol{s_i}\times\boldsymbol{\theta_1} + \boldsymbol{s_r^{sp}}\times(\mathbf{R}\boldsymbol{\theta_1})\right]\\ \boldsymbol{J_m}(\boldsymbol{M}) &= -E_i^0\,\boldsymbol{n}\times\left(\boldsymbol{\theta_1} + (\mathbf{R}\boldsymbol{\theta_1})\right).\end{aligned} \tag{18}$$

Separating the case where the aircraft is in front of the illuminated scatterer which can be considered as a reflection and the case where the aircraft is behind the illuminated scatterer by means of the principle of equivalence [40], the scattered field $\boldsymbol{E_s^{sh}}$ can be expressed as

$$\boldsymbol{E_s^{sh}} = \begin{cases} E_s^0\boldsymbol{\delta_b} & \text{if } \boldsymbol{s_r}\cdot\boldsymbol{n} \le 0\\ E_s^0\boldsymbol{\delta_r} & \text{otherwise,}\end{cases} \tag{19}$$

where

$$E_s^0 = j\frac{k_0 e^{-jk_0(R_1+R_2)}}{R_2}\sqrt{\frac{L_{\mathrm{H}} P_{TX} G_{TX}(\theta_1)\zeta_0}{2\pi\lambda^2}}\,LH\cdot \mathrm{sinc}\left(k_0\,UL/2\right)\mathrm{sinc}\left(k_0\,VH/2\right) \tag{20}$$

and

$$\begin{aligned}\boldsymbol{\delta_b} &= \boldsymbol{s_r}\times[\boldsymbol{s_r}\times\boldsymbol{n}\times\boldsymbol{s_i} - \boldsymbol{n}]\times\boldsymbol{\theta_1}\\ \boldsymbol{\delta_r} &= \boldsymbol{s_r}\times\left[\boldsymbol{s_r}\times\boldsymbol{n}\times\boldsymbol{s_r^{sp}} - \boldsymbol{n}\right]\times\mathbf{R}\boldsymbol{\theta_1}.\end{aligned} \tag{21}$$

Finally, the scattered field $\boldsymbol{E_s}$ of a smooth and heterogenous obstacle is given by

$$\boldsymbol{E_s} = \begin{cases} \sum_{\gamma=1}^{\Gamma} E_s^{0,\gamma}\,\boldsymbol{\delta_b^{\gamma}} & \text{if } \boldsymbol{s_r}\cdot\boldsymbol{n} \le 0\\ \sum_{\gamma=1}^{\Gamma} E_s^{0,\gamma}\,\boldsymbol{\delta_r^{\gamma}} & \text{otherwise.}\end{cases} \tag{22}$$

F. Analytical Expression of One Multipath Scattered Power P

From the analytical expression of the scattered field $\boldsymbol{E_s}$ in case of a smooth and heterogeneous scatterer (22), neglecting the polarization mismatch losses, the scattered power P generated by the illuminated scatterer at the airborne antenna output is given by

$$P = \frac{\|\boldsymbol{E_s}\|^2}{2\zeta_0} S_{\mathrm{eff}}^{\mathrm{AC}}, \tag{23}$$

where $S_{\mathrm{eff}}^{\mathrm{AC}}$ is the effective surface of the receiving airborne antenna,

$$S_{\mathrm{eff}}^{\mathrm{AC}} = \frac{\lambda^2}{4\pi} G_{RX}(\theta_2) \tag{24}$$

and G_{RX} is the received antenna gain assumed to be omnidirectional on the azimuth angle. Therefore,

$$P = \begin{cases} P^0\|\boldsymbol{\delta_b}\|^2 & \text{if } \boldsymbol{s_r}\cdot\boldsymbol{n} \le 0\\ P^0\|\boldsymbol{\delta_r}\|^2 & \text{otherwise,}\end{cases} \tag{25}$$

where P^0 is expressed as

$$P^0 = \frac{L_{\mathrm{H}} P_{TX} G_{TX}(\theta_1) G_{RX}(\theta_2)}{(2R_2\lambda)^2}(LH)^2 \times \left|\mathrm{sinc}\left(k_0\,UL/2\right)\right|^2\left|\mathrm{sinc}\left(k_0\,VH/2\right)\right|^2. \tag{26}$$

G. Discussion on the Proposed Approach

The MP scattered power P has been deterministically determined using PO (22). However, using this approach presents two major limitations for our AG channel model.

Limitation 1: Equation (22) implies to mesh the illuminated scatterer in a number Γ of elements, such that each element is smooth and homogeneous, and to sum the contribution of each elements to obtain the scattered field. However, meshing and summing over millions of illuminated scatterers would be too computationally expensive.

Limitation 2: Equation (22) requires the precise knowledge of all the details of all the scatterers illuminated for the study. However, no such knowledge is available for the high number of illuminated scatterers used in the analyzed scenarios.

Therefore, a statistical simplification of the PO approach for the determination of the scattered field is proposed to tackle both limitations.

IV. STATISTICAL SIMPLIFICATION OF THE PHYSICAL OPTICS APPROACH

The objective of this section is to provide a statistical simplification of PO to overcome both limitations introduced in section III.G. First, the addressing of the limitation 1, introducing the function h, is presented. Second, the handling of the limitation 2, using the ENAC campus building as a reference scatterer, is provided. Third, the analytical expression of the scattered power P using SSPO is introduced, and the necessary inputs needed from the illuminated scatterers to apply the proposed AG channel model are presented. Note that a numerical validation of SSPO is provided in Section VI.F.

A. Addressing Limitation 1

In this section, Limitation 1 is addressed by introducing a function h and an example of the determination of h is provided for the ENAC campus building.

Limitation 1 concerns the number of operations (summations and meshing) necessary to derive the electric field $\boldsymbol{E_s}$ in the case of a smooth and heterogenous scatterer expressed in (22). The computational complexity of such method becomes critical as the number of illuminated scatterers increases.

Therefore, to limit the number of necessary operations to derive $\boldsymbol{E_s}$, it is proposed to model the smooth and heterogenous scatterer as a smooth scatterer composed exclusively of the scatterer dominant material (metal, concrete, brick or wood) plus the glass windows by means of a simple function h: $\mathbb{R}^2 \rightarrow \mathbb{R}$. The function h is dependant on the dominant material and therefore one function h has to be determined per dominant material. Note that with this modelling, neither the meshing nor the sum are needed anymore since the scatterer is smooth and homogeneous (see equation (19)) and that only the function $|h|$ has to be determined. Using $|h|$, the targeted simplified scattered field is denoted as $\widetilde{\boldsymbol{E_s}}$ .The simplified field $\widetilde{\boldsymbol{E_s}}$ is expressed as

$$\widetilde{\boldsymbol{E_s}} = \begin{cases} \widetilde{E_s^0}\boldsymbol{\delta_b} & \text{if } \boldsymbol{s_r}\cdot\boldsymbol{n} \leq 0 \\ \widetilde{E_s^0}\boldsymbol{\delta_r} & \text{otherwise,} \end{cases} \tag{27}$$

with

$$\widetilde{E_s^0} = j\frac{k_0 e^{-jk_0(R_1+R_2)}}{R_2}\sqrt{\frac{L_H P_{TX} G_{TX}(\theta_1)\zeta_0}{2\pi\lambda^2}}LH\cdot \tag{28}$$

$$h\left(k_0\frac{UL}{2}, k_0\frac{VH}{2}\right).$$

Since P relies on the norm of $\boldsymbol{E_s}$ (see equation (23)), only $\left|\widetilde{E_s^0}\right|$ is needed to determine the power and thus only the absolute value of $|h|$ must be determined. For a scatterer, a function $|h|$ can be numerically determined by means of simulations knowing the exact composition of the scatterer equalizing (27) to (19) and taking the absolute value. Denoting $a = k_0\frac{UL}{2}$ and $b = k_0\frac{VH}{2}$ for clarity's purposes, $|h(a,b)|$ is simply given by

$$|h(a,b)| = \begin{cases} \dfrac{\|\boldsymbol{E_s}\|}{\frac{k_0 LH}{R_2}\sqrt{\frac{L_H P_{TX} G_{TX}(\theta_1)\zeta_0}{2\pi\lambda^2}}\|\boldsymbol{\delta_b}\|} & \text{if } \boldsymbol{s_r}\cdot\boldsymbol{n} \leq 0 \\ \dfrac{\|\boldsymbol{E_s}\|}{\frac{k_0 LH}{R_2}\sqrt{\frac{L_H P_{TX} G_{TX}(\theta_1)\zeta_0}{2\pi\lambda^2}}\|\boldsymbol{\delta_r}\|} & \text{otherwise.} \end{cases} \tag{29}$$

Note that the main limitation of this approach is that $|h|$ can only be simulated on a finite subset of $\mathbb{R}^2$. Therefore, for the value of a and b outside of this subset, a constant padding is applied to the $|h|$ function. Denoting $I^a = [a^{min}, a^{max}]$ and $I^b = [b^{min}, b^{max}]$ the intervals on which $|h(a,b)|$ has been determined, $|h|$ is obtained for any point of $\mathbb{R}^2$ as

$$|h(a,b)| = \left|h\left(\psi_a(a), \psi_b(b)\right)\right| \tag{30}$$

where

$$\begin{aligned} \psi_a(a) &= \begin{cases} \max(a, a^{min}) \text{ if } a < 0 \\ \min(a, a^{max}) \text{ otherwise} \end{cases} \\ \psi_b(b) &= \begin{cases} \max(b, b^{min}) \text{ if } b < 0 \\ \min(b, b^{max}) \text{ otherwise.} \end{cases} \end{aligned} \tag{31}$$

An example of the determination of $|h|$ for the ENAC campus building (see Fig. 4) is provided in the following, where the targeted $|h|$ function is denoted as $|h_{ec}|$. First, $|h_{ec}|$ is shown to be variable separable, which simplify its derivation. Then, $|h_{ec}|$ is derived by means of simulations and the shape of $|h_{ec}|$ is compared to the product of the sinc functions used for the smooth and homogeneous scatterer case (20).

Variable separability of $|h_{ec}|$: $|h_{ec}|$ is variable separable if and only if $\forall\, n \in \mathbb{N}^*$ every matrix $\mathbf{S}$ of the form

$$\mathbf{S} = \left(\left|h_{ec}(a_p, b_q)\right|\right)_{\substack{1\leq p\leq n \\ 1\leq q\leq n}} \tag{32}$$

has a rank equal to one, where a_p and b_q are discrete values. For this study, a simulation using (29) was performed to obtain a matrix $\mathbf{S}$ for $n = 8$ ($\mathbf{S} \in \mathcal{M}_8(\mathbb{R})$). It was found that the rank of the obtained matrix was one, with a tolerance threshold on

the singular values equal to 10^{-4}. Thus, $|h_{ec}|$ is considered variable separable. This is consistent with the smooth and homogeneous scatterer case (20), where $|h_{ec}(a,b)|$ is simply $|\mathrm{sinc}(a)||\mathrm{sinc}(b)|$.

Given the variable separability of $|h_{ec}|$, $|h_{ec}(a,b)|$ can be written as

$$|h_{ec}(a,b)| = \frac{|h_{ec}(a,0)||h_{ec}(0,b)|}{|h_{ec}(0,0)|}. \quad (33)$$

This property is also convenient regarding the number of simulations needed since $|h_{ec}|$ can be determined for a full rectangle subset of $\mathbb{R}^2$ by only performing simulations on two crossing line segments of $\mathbb{R}$.

Derivation of $|h_{ec}|$: Since $|h_{ec}|$ is variable separable, the shape of the four $|h_{ec}(a,0)|$ and the four $|h_{ec}(0,b)|$ functions (one per material) are derived separately. To obtain $|h_{ec}(a,0)|$ and $|h_{ec}(0,b)|$ (29), two simulations are performed in two different scenes: the horizontal scene and the vertical scene, that are detailed below.

The horizontal and the vertical scenes are shown in Fig. 6 and Fig. 7, respectively. Both scenes are composed of one DME/TACAN beacon (emitting at the L5 frequency), the ENAC campus building (simply referred to as "Scatterer" in Fig. 6 and Fig. 7) at a distance R_1 of the beacon and one moving aircraft. In both scenes, the aircraft is moving along a circular trajectory with constant radius R_2 centered at the center of the ENAC campus building. Note that, since the objective of the simulation is to investigate the field reradiated by the scatterer characterized by its function $|h_{ec}|$, and not the scatterer illumination, neither earth nor atmosphere have been considered in the simulation scene, and thus, the scatterer is always illuminated irrespective of the value of R_1 (the notion of RLOS does not exist in this simulation).

The distances R_1 and R_2 have been chosen to be equal to 60 and 40 km to be compliant with the far field condition, equal to 38.7 km for the ENAC campus building (9). Note that the $|h_{ec}(a,0)|$ and $|h_{ec}(0,b)|$ functions do not vary for any pairs of (R_1, R_2) above (38.7, 38.7) km.

In the horizontal scene (Fig. 6), the aircraft position is mathematically defined along the circular trajectory as $(R_2\cos(\phi_r), R_2\sin(\phi_r), 0)$, where the angle ϕ_r represents the angle from the horizontal specular reflection which ranges from $-\pi$ to π and $H_{ec} = 16.2$ m is the AGL height of the ENAC campus building facade. In this scene, the vectors $\boldsymbol{s_i}$ and $\boldsymbol{s_r}$ are contained in the plane $(x0y)$ and thus the dot product between $(\boldsymbol{s_r} - \boldsymbol{s_i})$ and $\boldsymbol{v} = \boldsymbol{z}$ is equal to zero. In other words, in the horizontal scene, V (17) is always equal to zero.

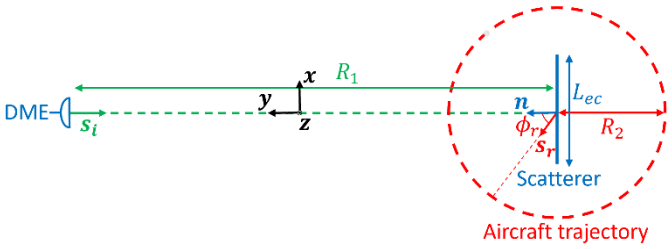

Fig. 6. Upper view of the horizontal scene.

Therefore, for each aircraft position, a value of $|h_{ec}(a,0)|$ is obtained. Note that since $\boldsymbol{s_i} \cdot \boldsymbol{x} = 0$, U is given by

$$U = \boldsymbol{s_r} \cdot \boldsymbol{x} = \sin(\phi_r) \in [-1,1], \quad (34)$$

and thus for the ENAC campus building, the interval I_{ec}^a is given by

$$\begin{aligned} a_{ec}^{min} &= -\frac{k_0^{L5} L_{ec}}{2} \\ a_{ec}^{max} &= \frac{k_0^{L5} L_{ec}}{2} \end{aligned} \Leftrightarrow I_{ec}^a = \left[-\frac{k_0^{L5} L_{ec}}{2}, \frac{k_0^{L5} L_{ec}}{2}\right], \quad (35)$$

where a_{ec}^{min} and a_{ec}^{max} are the minimum and maximum value in the horizontal plane where h_{ec} can be determined, k_0^{L5} is the wave number for the L5 frequency and $L_{ec} = 69.6$ m is the length of the ENAC campus building facade.

In the vertical scene (Fig. 7), the aircraft position is mathematically defined along the circular trajectory as $(0, R_2\cos(\theta_r), R_2\sin(\theta_r))$, where the angle θ_r represents the angle from the vertical specular reflection which ranges from $-\pi$ to π. In this scene, the vectors $\boldsymbol{s_i}$ and $\boldsymbol{s_r}$ are contained in the plane $(y0z)$ and thus the dot product between $(\boldsymbol{s_r} - \boldsymbol{s_i})$ and $\boldsymbol{u} = \boldsymbol{x}$ is equal to zero. In other words, in the vertical scene, U (17) is always equal to zero.

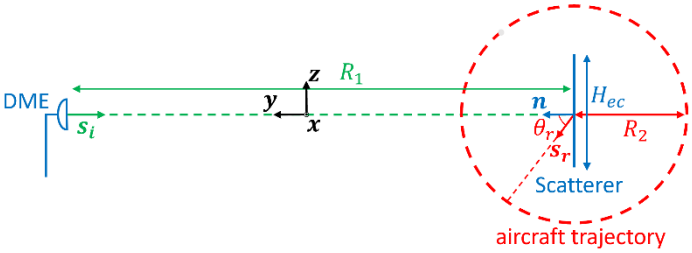

Fig. 7. Side view of the vertical scene.

Therefore, for each aircraft position, a value of $|h_{ec}(0,b)|$ is obtained. Note that since $\boldsymbol{s_i} \cdot \boldsymbol{z} = 0$, V is given by

$$V = \boldsymbol{s_r} \cdot \boldsymbol{z} = \sin(\theta_r) \in [-1,1], \quad (36)$$

and thus the interval I_{ec}^b is given by

$$\begin{matrix} b_{ec}^{min} = -\dfrac{k_0^{L5} H_{ec}}{2} \\ b_{ec}^{max} = \dfrac{k_0^{L5} H_{ec}}{2} \end{matrix} \Leftrightarrow I_{ec}^{b} = \left[-\frac{k_{0,L5} H_{ec}}{2}, \frac{k_{0,L5} H_{ec}}{2} \right], \quad (37)$$

where b_{ec}^{min} and b_{ec}^{max} are the minimum and maximum value in the vertical plane where h_{ec} can be determined and $H_{ec} = 16.2$ m is the AGL height of the ENAC campus building facade.

The two simulations are performed for the four possible materials (metal, concrete, brick and wood) in presence of glass windows and the simulated $|h_{ec}(a,0)|$ and $|h_{ec}(0,b)|$ functions using (29) are presented in Fig. 8 and Fig. 9 respectively, where only $-5° \leq \phi_r \leq 5°$ and $-20° \leq \theta_r \leq 20°$ are shown for visualization purposes.

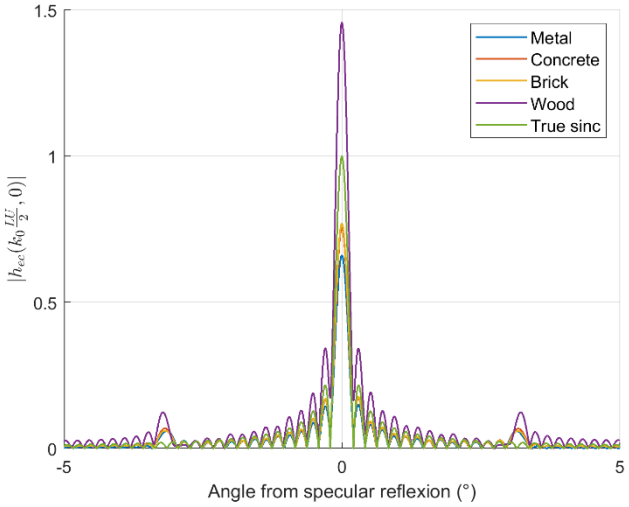

Fig. 8. $|h_{ec}(a,0)|$ for $-5° \leq \phi_r \leq 5°$ for the four possible dominant materials.

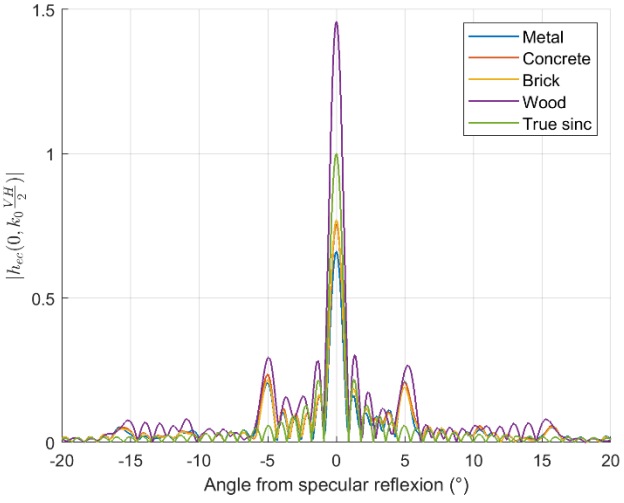

Fig. 9. $|h_{ec}(0,b)|$ for $-20° \leq \theta_r \leq 20°$ for the four possible dominant materials.

Three remarks can be made on the $|h_{ec}(a,0)|$ and $|h_{ec}(0,b)|$ functions:

1. They are similar to the sinc function which is consistent with the smooth and homogeneous case (20).
2. There are Grating Lobes (GL) due to the presence of the periodically distributed windows.
3. The highest peak of $|h_{ec}(a,0)|$ and $|h_{ec}(0,b)|$ can be smaller or greater than 1 depending on the material. However, $|h_{ec}(a,0)|$ and $|h_{ec}(0,b)|$ are later normalized by $|h_{ec}(0,0)|$ (33) and scaled by **R** (21) which both depend on the material. After the normalization and scaling, the maximum and minimum highest peaks are obtained for the metal and the wood, respectively. The values of $|h_{ec}(0,0)|$ for the 5 different materials is provided in the last column of Table I.

To summarize, both the $|h_{ec}(a,0)|$ and $|h_{ec}(0,b)|$ functions obtained in the case of the ENAC campus building can be seen as the sum of a background sinc function with a function g generating the GL.

B. Addressing Limitation 2

Limitation 2 concerns the precise knowledge of the composition of the facades. Since a very large number of illuminated scatterers have to be considered for the proposed AG propagation channel model, it is extremely challenging (if possible) to obtain such information.

Therefore, in this section, Limitation 2 is addressed by showing that for all the illuminated scatterers in the scenario, (28) can be used with the $|h|$ function of a single reference scatterer but customized for the illuminated scatterer dimensions, dominant material and a and b values from a statistical point of view, where a and b are calculated using the true dimension of the illuminated scatterer. First, it is shown that not only the $|h_{ec}|$ function from the ENAC campus building but any function $|h|$ from any rectangular illuminated scatterer is a sum of background sinc function with a function g generating the GL, where the positions, amplitudes and widths of the GL depend on the scatterer geometric parameters, by investigating the shape of $|h_{ec}|$ when the geometric parameters of the ENAC campus building are modified. Second, the importance of the positions, amplitudes and widths of the GL are discussed and the analysis concluded.

Influence of scatterer geometric parameters on the shape of $|h_{ec}|$: The geometric parameters being investigated are the scatterer length L and AGL height H, windows length L_{w} and height H_{w}, windows vertical and horizontal periodicities L_{p} and H_{p}. These parameters completely characterize the rectangular facades of a wide range of types of buildings considered in this study: facades composed of one dominant material plus glass windows. The minimum and maximum values, the step and the number of values N_{gp} considered for the geometric parameters are summarized in Table II. The initial set of geometric parameters of the ENAC campus

building is called the reference set and is provided in the last column of Table II for comparison purposes.

TABLE II
Range, step, number of values and reference set for the geometric parameters investigated.

Parameter	Min (m)	Max (m)	Step (m)	N_{gp}	Ref (m)
L	11.2	69.6	19.5	3	69.6
H	4.8	16.2	2.9	4	16.2
L_w	3.3	7.9	4.6	2	3.3
H_w	1.6	2.8	1.2	2	1.6
L_p	1.3	5.9	4.6	2	1.3
H_p	1.2	2.8	1.6	2	1.2

The range of values taken by the geometric parameters has been chosen to be representative of real life typical buildings with various size and number of windows. For example, the minimum set of geometric parameters (second column of TABLE II) corresponds to the dimension of the facade of a small hut that can be found in gardens or farms. The maximum set of geometric parameters (third column of TABLE II) is representative of the facade of large buildings that can be found in city centers. A set of geometric parameters in between the minimum and the maximum set easily represents a suburban facility.

Two simulations are performed each time a geometric parameter is modified from the initial set of parameters of the ENAC campus building. Then the impact on the shape of $|h_{ec}|$ is investigated. The two scenes considered for both simulations are the vertical and horizontal scenes presented in Fig. 6 and Fig. 7. For illustration purposes, Fig. 10 presents the $|h_{ec}(0,b)|$ normalized function for metal with (a) $H = 10.4$ m and (b) $H_p = 2.8$ m in comparison with the $|h_{ec}(0,b)|$ function of the ENAC campus building with its reference set of parameter. In addition, the perfect sinc function of a smooth and homogeneous scatterer with the dimension of the ENAC campus building is also displayed. Other simulations results are not shown in this paper for the sake of conciseness.

The simulation results show that the modification of the geometric parameters of the scatterers impacts the position, width and amplitude of the grating lobes but that both $|h_{ec}(a,0)|$ and $|h_{ec}(0,b)|$ functions can still be seen as the sum of a background sinc function with a function g generating the GL.

Therefore, it is assumed that not only the ENAC campus building but for any other rectangular facade with different set of geometric parameters, the functions $|h(a,0)|$ and $|h(0,b)|$ of this scatterer can be considered as a sum of a sinc function (which mainly depends on the scatterer AGL height and length) with another function representing the GL.

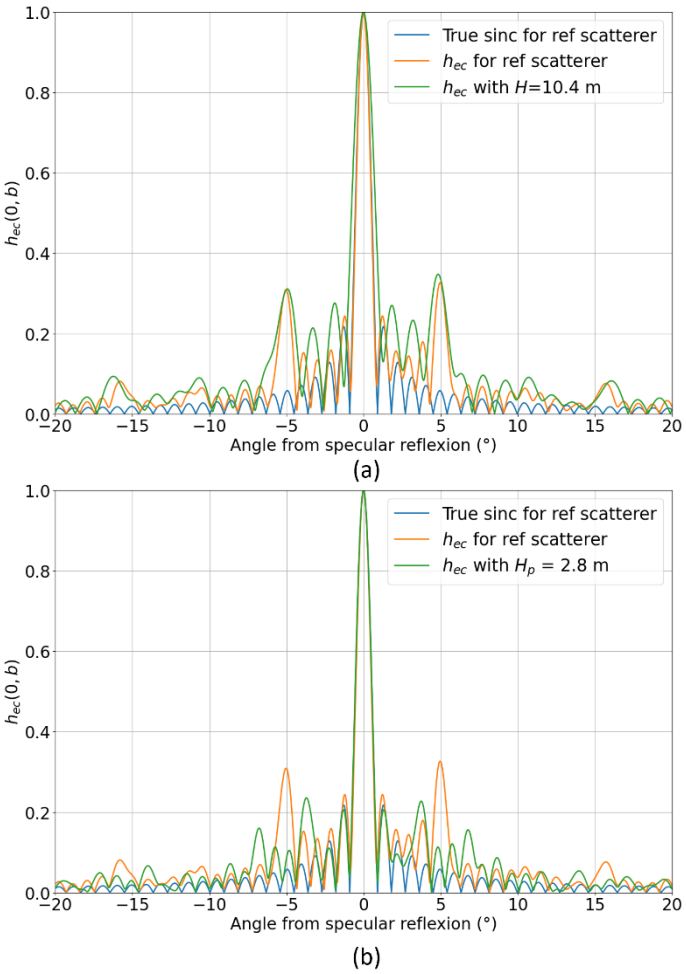

Fig. 10. $|h_{ec}(0,b)|$ normalized function for metal with (a) $H = 10.4$ m and (b) $H_p = 2.8$ m (in blue) in comparison with the $|h_{ec}(0,b)|$ function of the ENAC campus building (in orange) and a perfect sinc (in green).

Discussion: GL have three characteristics: position, width and amplitude. These parameters depend on the scatterer windows' height, length and horizontal and vertical periodicity [37] and therefore on the scatterer specific geometric parameters. However, considering the very high number of illuminated scatterers present in the scenario, all these illuminated scatterers are proposed to be represented by the $|h_{ec}|$ ENAC campus building from a statistical point of view, for 3 reasons:

1. With such a large number of illuminated scatterers, the horizontal orientation of the illuminated scatterers with respect to the DME and the aircraft can be assumed to be uniform on $[0,2\pi)$ and thus the positions of the GL in any $|h(a,0)|$ do not matter: the probability to fall into a GL is independent from the positions of the GL.
2. The vertical orientation of the illuminated scatterers cannot be assumed to be uniform on $[0,2\pi)$ given the configuration (obstacles are always assumed perpendicular to the ground). As shown in Fig. 10, the

position, width and amplitude of the GL changes when geometric parameters are modified. However, $|h_{ec}|$ is assumed to represent an average case.

3. The width and amplitude of the GL depend on the windows dimension and periodicity. Since the ENAC campus building windows are assumed to be representative of a typical building, the width and amplitude of the GL of ENAC campus building $|h_{ec}(a,0)|$ and $|h_{ec}(0,b)|$ functions are assumed to be representative of an average case.

Therefore, it is concluded that the ENAC campus building $|h_{ec}(a,0)|$ and $|h_{ec}(0,b)|$ functions can be used for any illuminated scatterer considered in the scenario from a statistical point of view. Combining this approach with the simplified scattered field $\widetilde{\boldsymbol{E_s}}$, the knowledge of the facades is no longer needed and thus both Limitation 1 and 2 have been addressed.

C. Scattered Power P and Necessary Inputs For The Propagation Channel Model

Combining the tackling of Limitation 1 and 2 and using equation (23), the scattered power P is updated into

$$P = \begin{cases} \widetilde{P^0}\|\boldsymbol{\delta_b}\|^2 & \text{if } \boldsymbol{s_r}\cdot\boldsymbol{n} \le 0 \\ \widetilde{P^0}\|\boldsymbol{\delta_r}\|^2 & \text{otherwise,} \end{cases} \tag{38}$$

with

$$\widetilde{P^0} = \frac{L_{\mathrm{H}} P_{TX} G_{TX}(\theta_1) G_{RX}(\theta_2)}{\lambda^2 R_2^2} (LH)^2 \cdot \frac{\left|h_{ec}\left(\psi_a\left(k_0\frac{UL}{2}\right),0\right)\right|^2 \left|h_{ec}\left(0,\psi_b\left(k_0\frac{VH}{2}\right)\right)\right|^2}{|h_{ec}(0,0)|^2}. \tag{39}$$

To summarize, after applying the SSPO approach, only four illuminated scatterers' inputs are necessary to determine the additional delay τ and the scattered power P necessary to completely determine the proposed propagation channel from a RFI impact analysis point of view:

1. The position of the center of the illuminated scatterers, that is needed to derive R_1, R_2 and many other parameters.
2. The dimensions L and H of the illuminated scatterers, that are directly used in (39).
3. The orientation of the illuminated scatterers, which is used in $\boldsymbol{\delta_b}$, $\boldsymbol{\delta_r}$ (21), U and V (17).
4. The material composition of the illuminated scatterers, which is needed for the derivation of $\mathbf{R}$ and the choice of $|h_{ec}|$.

Note that a numerical validation of SSPO is provided in Section VI.F.

V. METHODOLOGY FOR THE C/N_0 DEGRADATION CONSIDERING MP

In this section, the global methodology to derive the C/N_0 degradation in presence of MP for any aircraft position is presented. The methodology consists of 5 steps.

Step 1 – Determination of the Zones of Potential Illuminated Scatterers: The Zones of Potential Illuminated Scatterers (ZPIS) are defined as the geographical zones where illuminated scatterers can be found. Ideally, there should be only one ZPIS, defined as the entire earth surface. However, due to technical and computational constraints, smaller ZPIS may have to be defined to reduce the number of scatterers to be analyzed.

Step 2 - Determination of the Four Necessary Scatterers Inputs, Earth Relief and the Illuminated Scatterers Within the ZPIS: The four necessary inputs (position, dimensions, orientation and composition) of the scatterers and the earth relief within the ZPIS are determined from external sources such as large open access data bases. Note that some of the scatterers inputs might have to be stochastically generated, if the information is not provided in the available data bases.

Once the position and the dimensions of the scatterers and the earth relief within the ZPIS are known, R_1, R_2, $H_{\mathrm{DME}}^{\mathrm{AMSL}}$ and H^{AMSL} can be derived and the RLOS criteria (3) is applied. The scatterers within the ZPIS satisfying the RLOS criteria (3) are kept as the illuminated scatterers.

Step 3 – Determination of the Okumura-Hata Environment: From the position, length and orientation of the illuminated scatterers, the obstructed scatterers are identified. The non-obstructed scatterer are assumed to follow the Okumura-Hata open path loss as described in Section III.B. For the obstructed scatterers, the Okumura-Hata environment is arbitrary chosen after looking at the scatterer environment in external sources.

Step 4 - Application of the Proposed AG Channel Model: the proposed wideband AG channel model is applied to the illuminated scatterers within the RLOS of the visible DME/TACAN beacons. From the propagation channel, the additional delay with respect to the LOS of the MP τ (8) and the MP scattered power P (39) are retrieved for each of the illuminated scatterers.

Step 5 - Application of the C/N_0 Degradation Model Considering Multipath: the C/N_0 degradation model due to DME/TACAN considering MP developed in [5] is applied. The C/N_0 degradation is given in dB by

$$\left(\frac{C}{N_0}\right)_{deg} = 10\log_{10}\left(\frac{1-bdc}{1+R_I}\right), \tag{40}$$

where bdc is the blanking duty cycle,

$$bdc = 1 - e^{-2\sum_{m=1}^{M}\mu\left(\amalg_{q=1}^{Qm} B_{\mathrm{d},m}^{q}\right)\cdot PRF_m}, \tag{41}$$

with M the number of visible DME/TACAN beacons, μ the unidimensional Lebesgue measure, Q_m the number of disjoint blanked intervals generated by the visible beacon m, $B_{\mathrm{d},m}^{q} = \left[\mathrm{l}_{\mathrm{d},m}^{q}, \mathrm{r}_{\mathrm{d},m}^{q}\right]$ the m$^{\mathrm{th}}$ disjoint blanked interval and PRF_i the pulse repetition frequency for the visible beacon i. The below-blanker interfering signal-to-noise-ratio R_I is given by

$$R_I = \sum_{m=1}^{M} \frac{SSC(\Delta f_m) PRF_m \sqrt{\pi/\alpha}}{N_0 \beta_0} \sum_{n=1}^{N_m} P_m^n \left\{ 2\left(1 - \mathbf{1}_{I_m^{bdc}}(\tau_m^n)\right) + \sum_{q=1}^{Q_m} \left[\begin{array}{c} \mathrm{sign}\left(\tau_m^n - l_{\mathrm{d},m}^{q}\right) \mathrm{erfc}\left(\sqrt{\alpha}\left|l_{\mathrm{d},m}^{q} - \tau_m^n\right|\right) + \\ \mathrm{sign}\left(r_{\mathrm{d},m}^{q} - \tau_m^n\right) \mathrm{erfc}\left(\sqrt{\alpha}\left|r_{\mathrm{d},m}^{q} - \tau_m^n\right|\right) \end{array} \right] \right\}, \quad (42)$$

where SSC is the Spectral Separation Coefficient of beacon m, N_0 is the thermal noise power spectrum density level generated by the Radio-Frequency Front End (RFFE) block, β_0 is the thermal noise power degradation due to RFFE filter and correlator, N_m is the number of illuminated scatterers in the RLOS of visible beacon m, P_m^n and τ_m^n are the scattered power and the additional delay generated by illuminated scatterer n of visible beacon m respectively, $\mathbf{1}$ is the indicator function and $\mathrm{l}_{\mathrm{d},m}^{q}$ and $\mathrm{r}_{\mathrm{d},m}^{q}$ are the bounds of the total blanked interval generated by a received composite pulse from visible beacon m. The reader is referred to [5] for a more thorough explanation.

VI. APPLICATION TO JALTO AND TIXAK

In this section, the C/N_0 degradation due to DME/TACAN considering MP is derived by applying the methodology presented in section V at the two low altitude operational hot-spots defined during the RTCA Working Group 6 (WG6) activities [39]. The section is organized as follows. Section VI.A briefly introduces the criterion applied by the RTCA WG6 to identify the two altitude operational hot-spots. Section VI.B presents the ZPIS at the two altitude operational hot-spots. In Section VI.C the choices of definition of the four necessary inputs of the illuminated scatterers as well as the Okumura-Hata obstructed scatterers environment are introduced. Section VI.D and Section VI.E are dedicated to the presentation and analysis of the results obtained applying the proposed AG channel and C/N_0 degradation models. Finally, a validation of the proposed SSPO approach is provided in Section VI.F.

A. Identification of The Operational Low Altitude Hot-Spots

In the course of the RTCA WG6 activities, the operational low altitude hot spots for US and Europe have been determined finding the closest operational waypoint to the worst C/N_0 degradation due to DME/TACAN without considering MP at low altitude. Using this criterion, the following hot-spots were identified:

1. The US operational low altitude hot-spot: JALTO, flight altitude 2100ft AGL (altitude 640m), situated in Pennsylvania, near Philadelphia.
2. The European operation low altitude hot-spot: TIXAK, flight altitude 2000ft AGL (altitude 609m), situated in Germany, near Frankfurt.

B. Determination of The ZPIS at JALTO and TIXAK

To reduce the number of potential illuminated scatterers to be analyzed in these numerical examples, the ZPIS are defined as the states, or the countries, where at least one DME/TACAN beacon can be found in the RLOS of the aircraft for JALTO and TIXAK, respectively. A DME/TACAN beacon is said to be in the RLOS of the aircraft if the Euclidean distance between the beacon and the aircraft is below $RLOS\left(H_{\mathrm{AC}}^{\mathrm{AMSL}}, H_{\mathrm{DME}}^{\mathrm{AMSL}}\right)$ using (2) definition. At JALTO, the AMSL height of the DME/TACAN beacons' antenna $H_{\mathrm{DME}}^{\mathrm{AMSL}}$ is retrieved from a 2022 Federal Aviation Administration (FAA) database. At TIXAK, the height of the DME/TACAN beacons' antenna $H_{\mathrm{DME}}^{\mathrm{AMSL}}$ is retrieved from a 2022 EUROCONTROL database.

Under this rationale, 19 DME/TACAN beacons are identified inside the aircraft RLOS at JALTO. The identified DME/TACAN beacons are dispatched in 5 different states: 6 in Pennsylvania, 10 in New Jersey, 1 in New York, 1 in Delaware and 1 in Maryland, and thus, the ZPIS is simply defined as the union of the five states. Fig. 11 shows a map of the ZPIS at JALTO, where the aircraft is situated at the blue dot and the DME/TACAN beacons in the RLOS of the aircraft are represented by red dots.

At TIXAK, 13 DME/TACAN beacons are identified inside the aircraft RLOS. The DME/TACAN beacons are dispatched in 2 countries: 12 in Germany and 1 in Luxembourg and thus the ZPIS is simply defined as the union of the two countries. Fig. 12 shows a map of the ZPIS at TIXAK, where the aircraft is situated at the blue dot and the DME/TACAN beacons in the RLOS of the aircraft are represented by red dots.

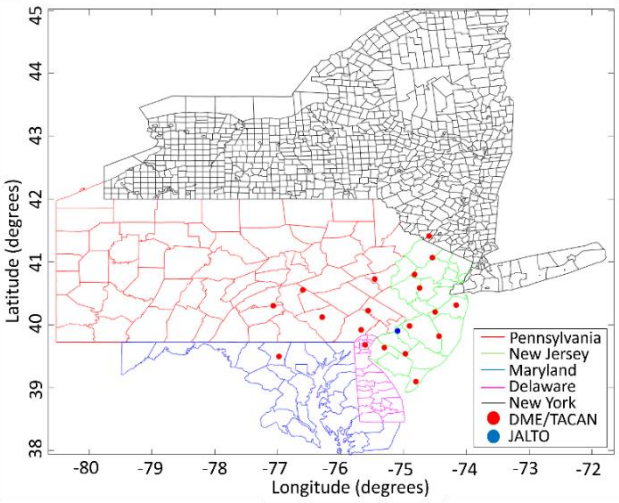

Fig. 11. ZPIS at JALTO, where the aircraft and the DME/TACAN beacons in the RLOS of the aircraft are represented by a blue and red dots, respectively.

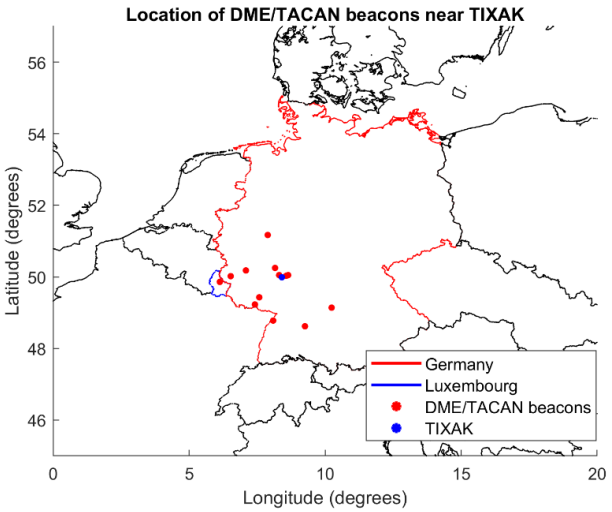

Fig. 12. ZPIS at TIXAK, where the aircraft and the DME/TACAN beacons in the RLOS of the aircraft are represented by a blue and red dots, respectively.

C. Determination of The Four Scatterers Inputs, the Illuminated Scatterers and Okumura-Hata environments

In this section, the determination of the four scatterer inputs, the illuminated scatterers within the ZPIS, and the Okumura-Hata environments of the illuminated scatterers, are presented.

Determination of the scatterers position, orientation and length within the ZPIS: For JALTO and TIXAK, the positions of the centers M, the unit vectors $(\boldsymbol{u}, \boldsymbol{v})$ characterizing the scatterers orientations and lengths L of the scatterers are retrieved from a worldwide computer-generated and publicly available database of the building footprints (horizontal plane projection only) released by Microsoft [42].

Determination of scatterers AGL height within the ZPIS: For both JALTO and TIXAK, the methodology to determine the illuminated scatterer AGL heights is as follows. If the AGL height of a illuminated scatterer is available from an open database, this retrieved height value is used for the simulations. For the other illuminated scatterers, where no database providing the AGL height is available, a unique height value is used: the mean of the building AGL height value retrieved from the literature for the considered country.

For JALTO, no database was found for the AGL height of the illuminated scatterers. Therefore, the value $H = 8$ m was chosen, which is just above the mean building AGL height found across the United-States [43]. Note that this value represents a tradeoff between the numerous country-side two-story building ($H \approx 5$ m) and the small amount of large ten-story buildings ($H \approx 30$ m) that can be found in city centers.

For TIXAK, an European publicly available database provided by Copernicus [44] was used to retrieve the AGL height H of the illuminated scatterers. Since the database only provides the AGL height of the scatterers within the core urban aeras, a AGL height of 5 m was chosen for the illuminated scatterers in suburban and rural aeras from the mean height values provided for Germany [45].

Determination of the illuminated scatterers within the ZPIS: For these numerical applications, since not all the information (AGL height, earth relief etc.) about the scatterers could be retrieved in the available data bases at the epoch of the manuscripts' writing, the methodology for finding the illuminated scatterers is simplified. The illuminated scatterers are defined in these numerical applications as the scatterers within the ZPIS that are in the RLOS of at least one DME/TACAN beacon identified in step 1; the RLOS of the DME/TACAN is derived from (2) always assuming that the AMSL heights of the DME/TACAN beacons and the scatterer are the AGL heights (earth relief equal to zero) and that the scatterer AGL height is 8 m. In total, more than 23 million and 15 million of illuminated building facades are found for JALTO and TIXAK, respectively.

Determination of the illuminated scatterers composition: The proposed AG channel model is intended to work with a database of the scatterers material composition. However, at the epoch of the article's writing, no accurate database was found for the scatterers composition for both JALTO and TIXAK. Therefore, for both hot spots, the composition of the illuminated scatterers are arbitrarily chosen through 5 different composition scenarios (CS) defined from the close observation of the visible DME/TACAN beacons surroundings in Google Maps. The 5 CSs have been designed to cover a wide range of (realistic) scatterers composition (CS 2 to CS 5) while also providing a potential worst case scenario where the largest number of illuminated scatterer dominant material is assumed to be metallic (CS 1).

The CSs are defined as a distribution of the scatterer materials. The distribution of the materials is used to randomly assign a material to each illuminated scatterer. Table III and Table IV provide the proposed distribution for the first four scenarios for JALTO and TIXAK, respectively. The main difference between JALTO and TIXAK CSs is that the wood is transformed into brick for TIXAK, since wood houses present in the US are not found in Europe where the brick is more often employed.

TABLE III
Material distribution for the first four scenarios, JALTO, where "Wd" stands for wood, "Crt" for concrete, "Mtl" for metal, "O-H" for Okumura-Hata and "S" for sub-urban.

	Length ≤ 50 m			Length > 50 m			O-H
	Wd (%)	Crt (%)	Mtl (%)	Wd (%)	Crt (%)	Mtl (%)	
CS 1	40	40	20	40	40	20	S
CS 2	45	45	10	45	45	10	S
CS 3	50	50	0	0	50	50	S
CS 4	50	50	0	0	70	30	S

TABLE IV
Material distribution for the first four scenarios, TIXAK, , where "Brk" stands for brick, "Crt" for concrete, "Mtl" for metal, "O-H" for Okumura-Hata and "S" for sub-urban.

	Length ≤ 50 m			Length > 50 m			O-H
	Brk (%)	Crt (%)	Mtl (%)	Brk (%)	Crt (%)	Mtl (%)	
CS 1	40	40	20	40	40	20	S
CS 2	45	45	10	45	45	10	S
CS 3	50	50	0	0	50	50	S
CS 4	50	50	0	0	70	30	S

In CS 1 and 2, there is no difference between the distribution for small ($L \leq 50$ m) and large ($L > 50$ m) obstacles for both JALTO and TIXAK. They are the simplest scenarios and the ones where the most metal is assumed to be present. Only a small change on the metal composition differentiates the two scenarios.

In CS 3 and 4, a difference is made between small and large obstacles for the compositions of the materials for both JALTO and TIXAK. This was deemed necessary since the largest scatterers are mostly made of concrete and metals (warehouses, commercial centers, hospitals, penitential centers, etc.) whereas smaller obstacles are mostly made of concrete, brick and wood (residential houses, small farms, etc.). Only a small change on the metal composition differentiates the two scenarios.

CS 5 is the most evolved scenario. It relies on the definition of four different zones for JALTO, and three zones for TIXAK. Each visible DME/TACAN beacon is assigned to a zone before running the simulations.

Zone 1 represents the urban environment. It is associated with large cities such as Philadelphia and Frankfurt for JALTO and TIXAK, respectively. The composition is mostly made of concrete and brick given the presence of large buildings.

Zone 2 represents the suburban environment. The composition is mostly made of wood for JALTO and brick for TIXAK given the presence of numerous houses in large residentials areas.

Zone 3 represents the rural environment. The composition is mostly made of wood for JALTO and brick for TIXAK given the dominance of allotments.

Zone 4 is only available for JALTO and represents the coastal environment. The scatterers are mostly made of wood.

Table IV and Table V provides the proposed distributions for the scenario 5 for JALTO and TIXAK, respectively.

TABLE V
Material distribution for scenario 5, JALTO, where "Wd" stands for wood, "Crt" for concrete, "Brk" for brick, "Mtl" for metal, "O-H" for Okumura-Hata, "U" for urban, "S" for sub-urban and "O" for open.

	Length ≤ 50 m				Length > 50 m				O-H
	Wd (%)	Crt (%)	Brk (%)	Mtl (%)	Wd (%)	Crt (%)	Brk (%)	Mtl (%)	
Z1	45	5	45	5	2	35	55	8	U
Z2	55	5	35	5	5	45	45	5	S
Z3	65	5	25	5	8	55	35	2	O
Z4	80	5	10	5	20	50	15	15	S

TABLE VI
Material distribution for scenario 5, TIXAK, where "Wd" stands for wood, "Crt" for concrete, "Brk" for brick, "Mtl" for metal, "O-H" for Okumura-Hata, "U" for urban, "S" for sub-urban and "O" for open.

	Length ≤ 50 m				Length > 50 m				O-H
	Wd (%)	Crt (%)	Brk (%)	Mtl (%)	Wd (%)	Crt (%)	Brk (%)	Mtl (%)	
Z1	5	65	25	5	2	65	25	8	U
Z2	5	55	35	5	5	55	35	5	S
Z3	5	45	45	5	8	45	45	2	O

Determination of the Okumura-Hata Environments: The Okumura-Hata environment of obstructed scatterers is defined for the 5 scenarios for both JALTO and TIXAK in the last column of Table III, Table IV, Table V and Table VI.

D. Application of the Proposed AG Channel Model

Knowing the four necessary inputs of each illuminated scatterer, the proposed AG channel model is applied to obtain the scattered power P (38) and the additional delay τ (8). Fig. 13 provides the scattered powers occurrence as a function of the additional delay with respect to the LOS signal Δ_τ obtained for the CS1 with (a) the beacon 5 and (b) the beacon 13 of JALTO, respectively. The blanking threshold (when visible) is represented by a red line. The number of illuminated scatterers N_m ($m = 5$ or $m = 14$) and LOS power are provided in the title.

Three remarks can be made regarding Fig. 13:

1. The power scattered by the obstacle is at least 20 dB and mostly around 100 dB below the LOS power. This is due to the Okumura-Hata path loss, the scattering and the $|h_{ec}|$ function as defined in Section IV.A.
2. Even if the scattered power generated by the individual scatterer is usually very weak, the number of illuminated scatterers is very high and an non negligible impact is expected on R_I.
3. When the LOS power is high (-98.6dBW for Fig. 13a), a very few number of scattered powers can be above the blanking threshold.

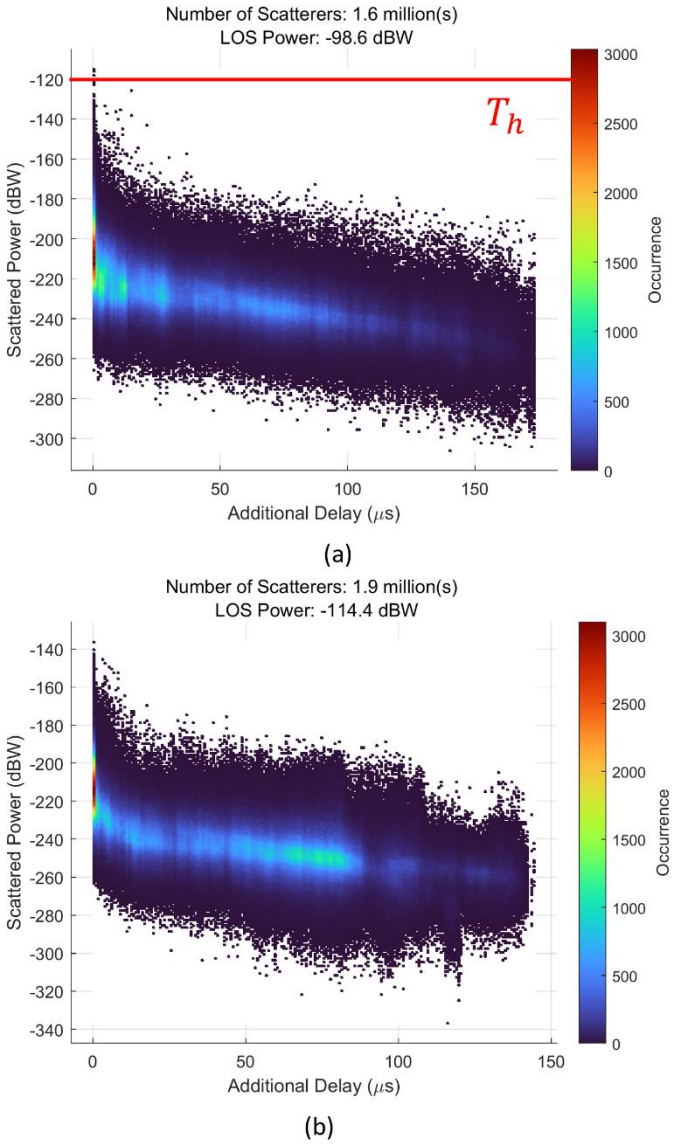

Fig. 13. scattered power occurrence over the additional delay obtained for CS1 with (a) the beacon 5 and (b) the beacon 13 of JALTO, respectively.

E. Application of the C/N_0 Degradation Model

With P and τ for every illuminated scatterers, R_I, bdc and the C/N_0 degradation due to DME/TACAN considering MP is obtained using equations (42),(41) and (40), respectively. Since the facades compositions are chosen randomly, the process is repeated 20 times and the mean and standard deviation (std) of R_I, bdc and C/N_0 are provided. These are the outputs usually given in the standards [1]. The results of the simulation are presented for JALTO in Table VII and Table VIII and for TIXAK in Table IX and Table X for $BW = 16$ MHz and $BW = 20$ MHz, respectively. The C/N_0 degradation in multipath-free conditions is presented in the last lines of Table VII and Table VIII for JALTO and Table IX and Table X for TIXAK for comparison purposes.

TABLE VII
C/N_0 degradation at JALTO considering MP, $BW = 16$ MHz

JALTO	R_I (-)		bdc (-)		$\left(\frac{C}{N_0}\right)_{deg}$ (dB)	
	Mean	std	Mean	std	Mean	std
Scenario 1	0.31	0.02	0.27	0.00	2.52	0.07
Scenario 2	0.30	0.02	0.27	0.00	2.51	0.05
Scenario 3	0.29	0.01	0.27	0.00	2.49	0.05
Scenario 4	0.29	0.02	0.27	0.00	2.48	0.04
Scenario 5	0.29	0.01	0.27	0.00	2.48	0.05
Without MP	0.16		0.27		2.00	

TABLE VIII
C/N_0 degradation at JALTO considering MP, $BW = 20$ MHz

JALTO	R_I (-)		bdc (-)		$\left(\frac{C}{N_0}\right)_{deg}$ (dB)	
	Mean	std	Mean	std	Mean	std
Scenario 1	0.31	0.03	0.32	0.00	2.82	0.08
Scenario 2	0.30	0.02	0.32	0.00	2.79	0.06
Scenario 3	0.30	0.01	0.32	0.00	2.78	0.04
Scenario 4	0.29	0.01	0.32	0.00	2.78	0.04
Scenario 5	0.30	0.01	0.32	0.00	2.79	0.04
Without MP	0.17		0.31		2.30	

TABLE IX
C/N_0 degradation at TIXAK considering MP, $BW = 16$ MHz

TIXAK	R_I (-)		bdc (-)		$\left(\frac{C}{N_0}\right)_{deg}$ (dB)	
	Mean	std	Mean	std	Mean	std
Scenario 1	0.23	0.03	0.19	0.00	1.80	0.08
Scenario 2	0.22	0.03	0.19	0.00	1.79	0.07
Scenario 3	0.22	0.02	0.19	0.00	1.78	0.05
Scenario 4	0.20	0.02	0.19	0.00	1.72	0.06
Scenario 5	0.20	0.01	0.19	0.00	1.71	0.05
Without MP	0.13		0.19		1.45	

TABLE X
C/N_0 degradation at TIXAK considering M, $BW = 20$ MHz

TIXAK	R_I (-)		bdc (-)		$\left(\frac{C}{N_0}\right)_{deg}$ (dB)	
	Mean	std	Mean	std	Mean	std
Scenario 1	0.22	0.02	0.23	0.00	1.98	0.05
Scenario 2	0.22	0.03	0.23	0.00	1.96	0.06
Scenario 3	0.22	0.03	0.23	0.00	1.96	0.06
Scenario 4	0.21	0.02	0.23	0.00	1.93	0.06
Scenario 5	0.21	0.00	0.23	0.00	1.94	0.05
Without MP	0.13		0.23		1.65	

Three conclusions are extracted from the results:

1. The range of the additional C/N_0 degradation generated by the DME/TACAN MP ranges from 0.48 to 0.52 dB at JALTO and from 0.16 to 0.35 dB at TIXAK, where less scatterers are illuminated.
2. The impact of the MP on bdc is almost always null, except for JALTO where it reaches at most 0.01. This means that very few building facades are generating a scattered power above the blanking threshold. Note that other scatterer types that could have triggered the blanker, such as electric pylons, have not been considered in this analysis.
3. R_I is the parameter most impacted by the consideration of MP due to the very high number of illuminated scatterers generating a scattered power below the blanking threshold.

F. Validation of SSPO

SSPO relies on a simplification of physical optics, in which a reference scatterer is used to infer the scattering of any facade. While the validity of PO has been widely studied [36], the proposed simplification in SSPO needs to be tested. Thus, SSPO is validated by comparing the PDP obtained at JALTO using the ENAC campus building façade, provided in Fig. 4 as the reference scatterer, to the PDP obtained using an alternative reference scatterer. For this validation, the alternative scatterer is chosen to be representative of a small house facade, with smaller dimensions than the ENAC campus building ones: the length and the width of the small house facade are set to $L_{sh} = H_{sh} = 5$ m, where "sh" stands for "small house", respectively. The small house facade is represented in Fig. 14.

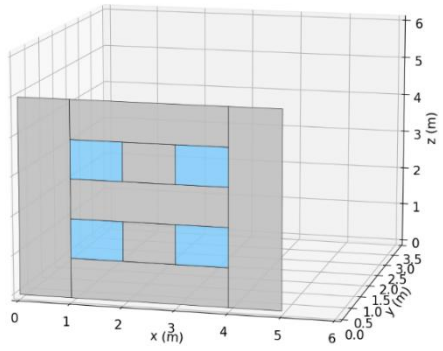

Fig. 14. Small house facade to be compared with the ENAC campus building. Grey: dominant material, blue: glass.

To obtain the PDP for the small house facade, first its function $|h|$ must be obtained. The function $|h|$ for the small house facade, $|h_{sh}|$, is determined following the methodology provided in Section IV.A. An important note for the small house facade is that the finite subset of $\mathbb{R}^2$ on which $|h_{sh}|$ can be determined is smaller that the finite subset for the ENAC campus building since $L_{sh} < L_{ec}$ and $H_{sh} < H_{ec}$, i.e., from (35) and (37),

$$\begin{matrix} L_{sh} < L_{ec} \\ H_{sh} < H_{ec} \end{matrix} \Leftrightarrow \begin{matrix} a_{ec}^{min} < a_{sh}^{min} \\ a_{ec}^{max} > a_{sh}^{max} \end{matrix} \text{ and } \begin{matrix} b_{ec}^{min} < b_{sh}^{min} \\ b_{ec}^{max} > b_{sh}^{max} \end{matrix} \quad (43)$$

where a_{sh}^{min} (b_{sh}^{min}) and a_{sh}^{max} (b_{sh}^{max}) are the minimum and maximum values where $|h_{sh}|$ can be determined in the horizontal (vertical) plane, respectively. Therefore, it is expected that using the small house facade as the reference scatterer, the constant padding defined in equation (30) will more often be triggered.

Once the function $|h_{sh}|$ is determined, the proposed AG channel model can be applied and the PDP for the CS1 with the DME/TACAN beacon 5 at JALTO is generated following the same methodology as Section VI.D. The PDP generated using the small house as the reference scatterer, $\mathrm{PDP}_{sh}(\tau, P)$, and the PDP generated the ENAC campus building as the reference scatterer, $\mathrm{PDP}_{ec}(\tau, P)$, shown in Fig. 13 (a), is compared by calculating $\mathrm{PDP}_{ec}(\tau, P) - \mathrm{PDP}_{sh}(\tau, P)$ for each pair (τ, P).

Fig. 15 provides (a) $\mathrm{PDP}_{sh}(\tau, P)$ for the CS1 with the DME/TACAN beacon 5 at JALTO and (b) $\mathrm{PDP}_{ec}(\tau, P) - \mathrm{PDP}_{sh}(\tau, P)$ for each pair (τ, P).

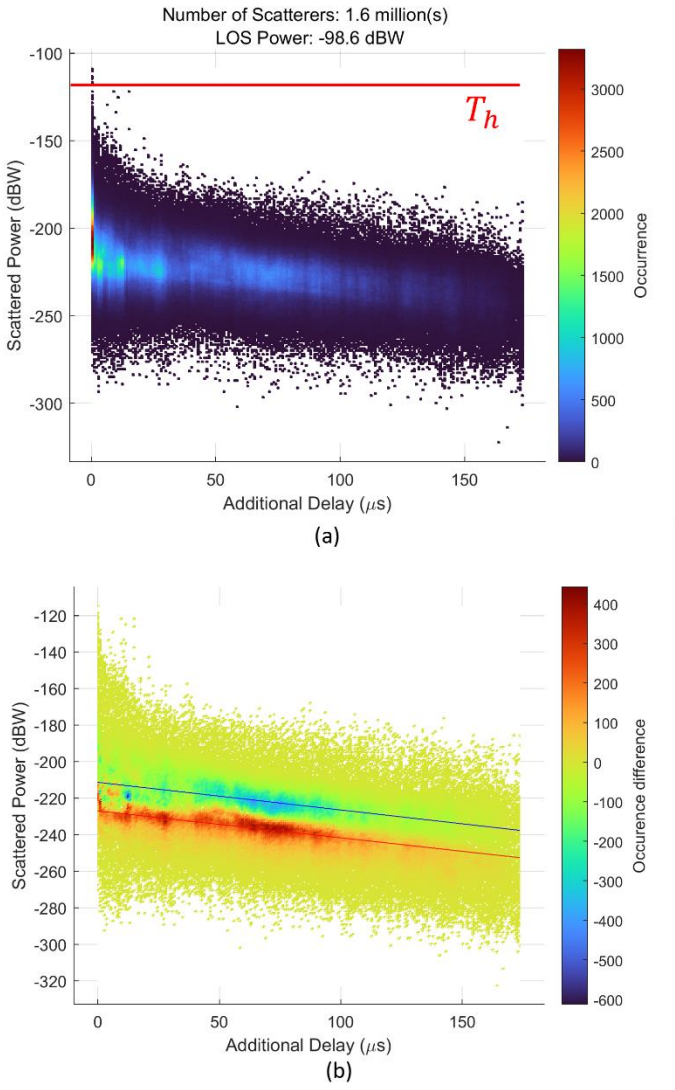

Fig. 15. (a) $\mathrm{PDP}_{sh}(\tau, P)$ for the CS1 with the DME/TACAN beacon 5 at JALTO and (b) $\mathrm{PDP}_{ec}(\tau, P) - \mathrm{PDP}_{sh}(\tau, P)$ for each pair (τ, P). The straight blue and red lines in (b) are the straight lines obtained by linear regression of the blue and red scatter of points, respectively.

Two observations can be deduced from Fig. 15:

1. Fig. 15 (a) shows that the shape of the PDP using the small house facade as the reference scatterer $\mathrm{PDP}_{sh}(\tau, P)$ is almost the same as the PDP using the ENAC campus building as the reference scatterer $\mathrm{PDP}_{ec}(\tau, P)$ shown in Fig. 13 (a).
2. Fig. 15 (b) shows that while the shape of the two PDPs is almost the same, there are less occurrences for $\mathrm{PDP}_{ec}(\tau, P)$ for high values of P (red scatter of points) than for low values of P (blue scatter of points). This effect occurs because the constant padding is more often triggered in the small house case, which represent a worst case from a scattered power point of view. Indeed, the blue and red straight lines obtained by applying a linear regression of the blue and red scatter of points shown in Fig. 15 (b) show the same slope equal to -0.14, and thus are separated by a constant offset equal to 14.2 dB which is close to the offset between the constant padding values $|h_{ec}(a_{ec}^{max}, 0)|^2$ and $|h_{sh}(a_{sh}^{max}, 0)|^2$, equal to 13.6 dB. Note that the different FSL due to the different ray delays values on the scatterers triggering the padding is represented by the slope of the linear regressions.

Finally, from these two observations, the use of SSPO approach instead of PO approach to model the scatterer illumination when considering such a large number of scatterers is validated. Moreover, the second observation further justifies the choice of a large scatterer as the reference scatterer, as it is the case for the ENAC campus building.

VII. CONCLUSION

In this article, a new hybrid deterministic-stochastic geometrically based wideband AG propagation channel model have been proposed. The proposed AG model includes an analytical formula for the additional delay, an Okumura-Hata path loss for the scatterer illumination and the mathematical expression of the scattered power generated by the illuminated scatterers using a statistical simplification of PO to allow the model to cope with very large numbers of illuminated scatterers present in the scenarios. After the application of the SSPO approach, only four inputs are needed from the illuminated scatterers to apply the proposed AG model: the position, dimension, orientation and composition.

Combining the proposed channel model with the C/N_0 degradation model presented in Part I [5], the general methodology to determine the C/N_0 due to DME/TACAN considering MP have been determined. To illustrate the application of these models, the analysis of two cases of study, JALTO, in the US, and TIXAK, in Europe, have been conducted. In this article, the AGL heights of the illuminated scatterers have been determined from dataset when available, or using a representative mean value when not. and, although the channel model is intended to work with a deterministic environment, the compositions of the scatterers have been statistically determined due to the lack of information about illuminated scatterers materials composition. Note that this statistic element is to be removed as soon as precise databases concerning the illuminated scatterers material composition are available. Results have shown that the consideration of MP adds to the $C/N0$ degradation due to DME/TACAN from 0.48 to 0.52 dB and from 0.16 to 0.35 dB at JALTO and TIXAK (where less scatterers are illuminated), respectively.

It must be highlighted that the proposed AG channel is neither restricted to the RFI analysis, since the CIR time series can almost be generated (accounting for a phase mathematical model) nor to the DME/TACAN system; the proposed AG channel model could indeed be applied to any other system composed of a ground emitter and a sky receiver operating in the L-band.

Future works include the study of OLOS scenarios for the beacon-to-airborne GNSS antenna and scatterer-to-airborne GNSS antenna paths.

REFERENCES

[1] RTCA, "DO 292 - Assessment of Radio Frequency Interference Relevant to the GNSS L5/E5A Frequency Band," Jul. 2004.

[2] F. Bastide, C. Macabiau, D. Akos, and B. Roturier, "Assessment of L5 Receiver Performance in Presence of Interference Using a Realistic Receiver Simulator," in *16th International Technical Meeting of The Satellite Division of the Institute of Navigation*, Portland, Oregon, Sep. 2003.

[3] C. Hegarty, T. Kim, S. Ericson, P. Reddan, T. Morrissey, and A. J. Van Dierendonck, "Methodology for Determining Compatibility of GPS L5 with Existing Systems and Preliminary Results," presented at the Proceedings of The Institute of Navigation Annual Meeting, Cambridge, MA, Jun. 1999.

[4] C. Hegarty, A. J. Van Dierendonck, D. Bobyn, M. Tran, T. Kim, and J. Grabowski, "Suppression of Pulsed Interference through Blanking," presented at the Proceedings of the Institute of Navigation Annual Meeting, Fairvax, VA, Jun. 2000.

[5] N. Gault, A. Garcia-Pena, A. Chabory, C. Macabiau, and L. Shi-Garrier, "DME/TACAN Multipath Impact on GNSS L5/E5a Airborne Receivers Part I: C/N0 Degradation Model," *IEEE Trans. Aerosp. Electron. Syst.*, submitted.

[6] D. W. Matolak and R. Sun, "Unmanned aircraft systems: Air-ground channel characterization for future applications," *IEEE Trans. Veh. Technol.*, vol. 10, pp. 79–85, 2015.

[7] A. Altaf Khuwaja, Y. Chen, N. Zhao, M.-S. Alouini, and P. Dobbins, "A Survey of Channel Modeling for UAV Communications," IEEE Communications Surveys & Tutorials, Vol. 20, No. 4, Fourth Quarter 2018.

[8] J. Khawara, I. Guvenc, D. W. Matolak, U.-C. Fiebig, and N. Scheckenburger, "A survey of air-to-ground propagation channel modeling for unmanned aerial

vehicles," *IEEE Commun. Surveys Tuts.*, vol. 21, no. 3, pp. 2361–2391, 3rd Quart 2019.

[9] C. Yan, J. Zhang, and J. Wang, "A Comprehensive Survey on UAV Communication Channel Modeling," *IEEE Access*, vol. 7, pp. 107769–107792, 2019.

[10] J. Rodriguez-Piñeiro, T. Dominguez-Bolaño, X. Cai, Z. Huang, and X. Yin, "Air-to-Ground Channel Characterization for Low-Height UAVs in Realistic Network Deployments," *IEEE Trans. Antennas Propag.*, vol. 69, no. 2, pp. 992–1006, Feb. 2021.

[11] Z. Cui, K. Guan, C. Oestges, C. Briso-Rodriguez, B. Ai, and Z. Zhong, "Cluster-based Characterization and Modeling for UAV Air-to-Ground Time-Varying Channels," *IEEE Trans. Veh. Technol.*, vol. 71, no. 7, pp. 6872–6883, Jul. 2022.

[12] D. Mielke, M. Walter, M. Bellido-Manganell, and U.-C. Fiebig, "Application of Path-Based Multipath Component Tracking on Air-Ground Channel Measurement Data," *IEEE Trans. Antennas Propag.*, vol. 72, no. 5, pp 5546–5559, Jan. 2023.

[13] M. Pang, Q. Zhu, C.-X. Wang, Z. Lin, C. Lv, and Z. Li, "Geometry-Based Stochastic Probability Models for the LoS and NLoS Paths of A2G Channels Under Urban Scenarios," *IEEE Internet Things J.*, vol. 10, no. 3, pp. 2360–2372, Oct. 2022.

[14] G. Sun *et al.*, "A 3D Wideband Channel Model for RIS-Assisted MIMO Communications," *IEEE Trans. Veh. Technol.*, vol. 71,no. 8, Aug. 2022.

[15] H. Jiang, B. Xiong, and E. Basar, "Physics-based 3D end-to-end modeling for double-RIS assisted non-stationary UAV-to-ground communication channels," *IEEE Trans. Commun.*, vol. 71, no. 7, pp. 4247–4261, Apr. 2023.

[16] D. W. Matolak and R. Sun, "Air–ground channel characterization for unmanned aircraft systems—Part I: Methods, measurements, and models for over-water settings," *IEEE Trans. Veh. Technol.*, vol. 66, no. 1, pp. 26–44, Jan. 2017.

[17] D. W. Matolak and R. Sun, "Air–ground channel characterization for unmanned aircraft systems—Part II: Hilly and mountainous settings," *IEEE Trans. Veh. Technol.*, vol. 66, no. 3, pp. 1913–1925, Mar. 2017.

[18] D. W. Matolak and R. Sun, "Air-ground channel characterization for unmanned aircraft systems—Part III: The suburban and near-urban environments," *IEEE Trans. Veh. Technol.*, vol. 66, no. 8, pp. 6607–6618, Aug. 2017.

[19] N. Scheckenburger *et al.*, "Measurement of the L-band air-to-ground channel for positioning applications," *IEEE Trans. Aerosp. Electron. Syst.*, vol. 52, no. 5, pp. 2281–2297, Oct. 2016.

[20] N. Scheckenburger, T. Jost, M. Walter, G. Del Galdo, D. W. Matolak, and U.-C. Fiebig, "Wideband Air-Ground Channel Model for a Regional Airport Environment," *IEEE Trans. Veh. Technol.*, vol. 68, no. 7, pp. 6243–6256, Jul. 2019.

[21] E. Haas, "Aeronautical channel modeling," *IEEE Trans. Veh. Technol.*, vol. 51, no. 2, pp. 254–264, Mar. 2002.

[22] A. Al-Hounani, S. Kandeepan, and A. Jamalipour, "Modeling Air-to-Ground Path Loss for Low Altitude Platforms in Urban Environments," presented at the Proc. IEEE Global Commun. Conf. (GLOBECOM), Austin, TX, USA, 2014, pp. 2898–2904.

[23] W.-G. Newhall and J. H. Reed, "A geometric air-to-ground radio channel model," presented at the Proc. IEEE Military Commun. Conf. (MILCOM), Anaheim, CA, USA, Oct. 2002, pp. 632–636.

[24] M. Ibrahim and H. Arslan, "Air-ground Doppler-delay spread spectrum for dense scattering environments," presented at the Proc. IEEE Military Commun. Conf. (MILCOM), Tempa, FL, USA, Oct. 2015, pp. 1661-1666.

[25] N. Scheckenburger, T. Jost, D. Shutin, M. Walter, G. Del Galdo, and U.-C. Fiebig, "Reflector localization for geometrical modeling the air–ground channel," *IEEE Trans. Veh. Technol.*, vol. 67, no. 9, pp. 7994–8008, Sep. 2018.

[26] N. Scheckenburger, "Wideband Air-Ground Channel Model for a Regional Airport Environment," Ph.D dissertation, Fakultät für Elektrotechnik und Informationstechnik, Illmenau, Germany, 2017.

[27] A. Chen, "Development of a Hybrid Deterministic-Statistical GPS Multipath Simulator for Airport Navigation," PhD Thesis, Institut National Polytechnique de Toulouse, 2011.

[28] M. Ait Ighil, "Enhanced physical-statistical simulator of the land mobile satellite channel for multipath modelling applied to satellite navigation systems," Institut Supérieur de l'Aéronautique et de l'Espace (ISAE), Toulouse, France, 2013.

[29] M. Ait-Ighil *et al.*, "Simplifying the propagation environment representation for LMS channel modelling," *EURASIP J. Wireless Commun. Netw.*, vol. 1, pp. 1–20, Mar. 2012.

[30] N. Gault, A. Garcia-Pena, A. Chabory, and C. Macabiau, "Impact of DME/TACAN on GNSS L5/E5a Receiver at Low Altitude Considering Multipath," presented at the Proceedings of the 35th International Technical Meeting of the Satellite Division of the Institute of Navigation (ION GNSS+ 2022), Denver, Sep. 2022.

[31] ICAO, *European Guidance Material on Managing Building Restricted Aeras*, Third Edition. 2015.

[32] M. Hata, "Empirical Formula for Propagation Loss in Land Mobile Radio Services," *IEEE Trans. Veh. Technol.*, vol. 29, no. 3, pp. 317–325, Aug. 1980.

[33] F. Perez-Fontan and P. M. Espiñeira, *Modelling the Wireless Propagation Channel: A simulation approach with MATLAB*. Wiley, 2008.

[34] ITU-R P834-9, *Effects of tropospheric refraction on radiowave propagation*. 2017.

[35] L. Diaz and T. Miligan, *Engineering Using Physical Optics. Practical CAD Techniques and Software*. in Artech House. 1996.

[36] A. Steingass, A. Lehner, F. Perez-Fontan, E. Kubista, and B. Arbesser-Rastburg, "Characterization of the

aeronautical satellite navigation channel through high-resolution measurement and physical optics simulation," *Int. J. Satell. Commun. Netw.*, vol. 26, pp. 1–30, 2008.
[37] H. Visser, *Antenna Theory and Applications*. Wiley, 2012.
[38] A Von Hippel, *Les diélectriques et leurs applications*. in Dunod. 1961.
[39] A. Chabory, "Modélisation Electromagnétique des radômes par des techniques basées sur les faisceaux gaussiens," Paul Sabatier University, Toulouse, France, 2004.
[40] R. F. Harrington, *Time–Harmonic Electromagnetic Field*. in Wiley. 1961.
[41] "RTCA Special Committees 159." [Online]. Available: https://www.rtca.org/sc-159/
[42] Microsoft Maps, "Worldwide building footprints." [Online]. Available: https://github.com/microsoft/GlobalMLBuildingFootprints
[43] L. Mengmeng, E. Koks, H. Taubenböck, and J. Ven Vliet, "Continental-scale mapping and analysis of 3D building structure," *Remote Sens. Environ.,* vol. 264, preprint no. 111859, 2020.
[44] Copernicus, "Urban Atlas Building Height 2012 (raster 10 m), Europe - version 3." [Online]. Available: https://doi.org/10.2909/42690e05-edf4-43fc-8020-33e130f62023
[45] D. Frantz *et al.*, "National-scale mapping of building height using Sentinel-1 and Sentinel-2 time series," *Remote Sensing of Environment 252, 112128*, 2021.

Nicolas Gault received the double M.Sc. degree in electrical engineering and aerospace systems from ENAC, the French Civil Aviation University, Toulouse, France, in 2020. He is now a Ph.D student at the TELECOM lab of ENAC. He is currently working toward the Ph.D. degree in applied mathematics, signal processing and electromagnetism at the French Civil Aviation University, Toulouse, France. He recently spent 6 months at the RF & SatNav laboratory of the University of Colorado, Boulder, for collaborative research.

Alexandre Chabory received the M.Sc. degree in electrical engineering from ENAC, the French Civil Aviation University, Toulouse, in 2001, and the Ph.D. degree in electromagnetism and micro-waves from Paul Sabatier University, Toulouse, in 2004. From 2004 to 2007, he was a Post-Doctoral Scientist with the Eindhoven University of Technology, the Netherlands. Since 2007, he has been with ENAC where he is now full-professor and head of the electromagnetics and antennas research group. His research interests include electromagnetic theory and modeling, mainly for aeronautical applications.

Axel Garcia-Pena is a researcher/lecturer with the SIGnal processing and NAVigation (SIGNAV) research axis of the TELECOM lab of ENAC (French Civil Aviation University), Toulouse, France. His research interests are GNSS navigation message demodulation, optimization and design, GNSS receiver design and GNSS satellite payload. He received his double M.Sc. degree in 2006 in digital communications from SUPAERO and UPC (Universidad Politécnica de Cataluña), and his Ph.D. degree in 2010 in mathematics, computer science and telecommunications from the INPT (Polytechnic National Institute of Toulouse), France.

Christophe Macabiau received the M.Sc. degree in electrical engineering from ENAC, the French Civil Aviation University, Toulouse, in 1994, and the Ph.D. degree in signal and image processing fom the INPT, Toulouse, France, 1997. Since 1997, he has been working on the application of satellite navigation techniques to civil aviation. He has been in charge of the signal processing lab of ENAC since 2000, where he also started dealing with navigation techniques for terrestrial navigation. He is currently the head of the TELECOM team of ENAC, that includes research groups on signal processing and navigation, electromagnetics, and data communication networks.